A. COVER PAGE

Project Title: Novel gas chromatography for rapid, in situ workplace hazardous VOC/VIC analysis	
Grant Number: 5R01OH011082-04	**Project/Grant Period:** 09/01/2018 - 08/31/2022
Reporting Period: 09/01/2021 - 08/31/2022	**Requested Budget Period:** 09/01/2021 - 08/31/2022
Report Term Frequency: Final	**Date Submitted:** 10/05/2023
Program Director/Principal Investigator Information: XUDONG FAN , PHD MS BS **Phone Number:** 734-763-1273 **Email:** xsfan@umich.edu	**Recipient Organization:** UNIVERSITY OF MICHIGAN AT ANN ARBOR 3003 SOUTH STATE STREET 1st Floor Wolverine Tower ANN ARBOR, MI 481091276 **DUNS:** 073133571 **UEI:** GNJ7BBP73WE9 **EIN:** 1386006309A1 **RECIPIENT ID:**
Change of Contact PD/PI: NA	
Administrative Official: PATRICK CASE 3003 South State Street Ann Arbor, MI 481091274 **Phone number:** 734-764-7248 **Email:** pcase@umich.edu	**Signing Official:** KAREN R SAMPSON 3003 South State Street Ann Arbor, MI 481091274 **Phone number:** 734-764-8240 **Email:** ksampson@umich.edu
Human Subjects: NA	**Vertebrate Animals:** NA
hESC: No	**Inventions/Patents:** Yes **If yes, previously reported:** Yes

B. ACCOMPLISHMENTS

B.1 WHAT ARE THE MAJOR GOALS OF THE PROJECT?

The goal of the project is to develop an automated portable multi-dimensional gas chromatography (GC) device that rapid and in-site analysis of volatile organic and inorganic compounds (VOCs/VICs). There are 5 specific aims:
Aim 1: Design, micro-fabricate, characterize, and optimize the components for multi-dimensional micro-GC.
Aim 2: Assemble the multi-dimensional micro-GC device and develop operation/analysis algorithm.
Aim 3: Integrate an automated VIC detection module.
Aim 4: Characterize and optimize the multi-dimensional micro-GC device, and create a VOC/VIC reference library.
Aim 5: Field-test the multi-dimensional micro-GC device and benchmark against conventional industrial hygiene methods

B.1.a Have the major goals changed since the initial competing award or previous report?

No

B.2 WHAT WAS ACCOMPLISHED UNDER THESE GOALS?

File Uploaded : Accomplishments.pdf

B.3 COMPETITIVE REVISIONS/ADMINISTRATIVE SUPPLEMENTS

For this reporting period, is there one or more Revision/Supplement associated with this award for which reporting is required?

No

B.4 WHAT OPPORTUNITIES FOR TRAINING AND PROFESSIONAL DEVELOPMENT HAS THE PROJECT PROVIDED?

NOTHING TO REPORT

B.5 HOW HAVE THE RESULTS BEEN DISSEMINATED TO COMMUNITIES OF INTEREST?

NOTHING TO REPORT

B.6 WHAT DO YOU PLAN TO DO DURING THE NEXT REPORTING PERIOD TO ACCOMPLISH THE GOALS?

Not Applicable

Accomplishments

Below are summaries of what we have accomplished in the past two years. We will describe the progress that we made in four aspects. (1) Component level; (2) System level; (3) Data analysis algorithm development; (4) Technology translation.

1. Component level: Ultrathin silica integration for enhancing reliability of microfluidic photoionization detectors

In the past, we have developed microfluidic photoionization (μPID) and helium dielectric barrier discharge PID, both of which have been reported previously. Here, we focus more on addressing a long-standing practical issue related to the lifetime of a μPID.

Microfluidic photoionization detectors (μPID) based on silicon chips are able to rapidly and sensitively detect volatile compounds. However, the applications of μPID are limited by the manual assembly process that involves using a glue that may potentially outgas and clog the fluidic channel, and by the short lifetime of the vacuum ultraviolet (VUV) lamps (especially, Argon lamps). Here, we developed a gold-gold cold welding-based microfabrication process to integrate ultrathin (10 nm) silica into μPID. The silica coating not only enables direct bonding of the VUV window to silicon under amicable conditions, but also works as a moisture and plasma exposure barrier for VUV windows (*i.e.*, MgF_2 and LiF) that are highly susceptible to hygroscopicity and solarization. This work will lead to future development of a new type of VUV lamps and the corresponding μPIDs that can be mass produced with a high yield. It will also help enhance the reliability of PIDs in general with a longer lifetime and better regenerability.

Figure 1(A) depicts a generic device structure of a silica-integrated microfluidic photoionization detector (SIPID). To protect the VUV window, an interlayer was formed by coating silica on the VUV window surface facing the microfluidic channel, i.e., the side exposed to ambient moisture and VOC analytes during detection. The interlayer was then integrated onto the microfluidic chip through gold-gold cold-welding using lithographically-patterned gold as the intermediate adhesive layer. Note that the counter gold layer on the microfluidic chip also serves the electrode contacts accessible for wire bond packaging. As an example, Figures 1(B) and (C) show a 10 nm-silica-coated MgF_2 window integrated microfluidic chip with the full microfabrication process illustrated in Figure 1(D). Detailed descriptions of the fabrication processes are given in “Materials and Methods”.

Unlike traditional hermetic bonding methods (e.g., anodic and eutectic) that require high temperatures (>300 ^oC) for long periods (>1 hour), cold welding allows for a low-temperature (150 ^oC) bonding process in a short time (10 minutes) to prevent the cracking of VUV windows due to their large mismatch in their thermal expansion coefficients (CTE) with silicon. On the other hand, compared to other low-temperature bonding techniques (e.g., polymer bonding) that cannot achieve a hermetic seal due to the gas permeable nature of most polymers, the gold cold-welded interface in the SIPID provides a leak-free encapsulation that can sustain a flow rate up to 40 mL/min, which is sufficient for most applications in gas chromatography.

The commercial PID lamp, which comes with a 1 mm thick built-in VUV window (MgF_2 for a Kr lamp and LiF for an Ar lamp) was then mechanically attached on top of the integrated interlayer using UV curable glue along the lamp’s circumferential edge such that both the bottom surface of the lamp’s built-in VUV window and the top surface of the interlayer VUV window are sealed from ambient. Note that although the glue was still used here for simplicity and convenience, unlike our previous design, in the current design, the VUV lamp was easily attached to the top of the interlayer and the glue was no longer in contact with the microfluidic chip beneath, and therefore, potential outgassing and clogging issues are avoided. Other packaging techniques (e.g., 3D printing) can also be employed to make a lamp fixture and completely avoid using glue if needed.

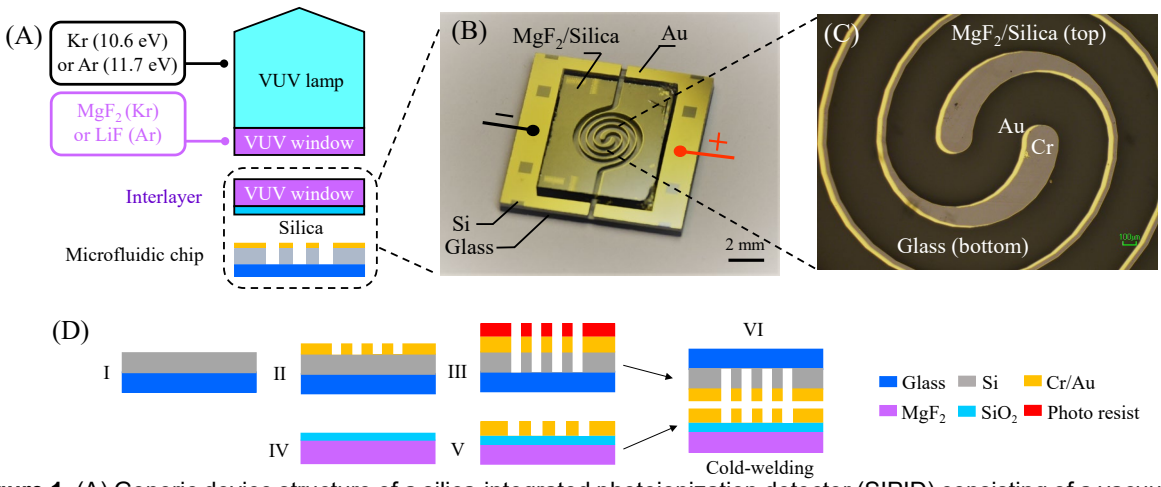

Figure 1. (A) Generic device structure of a silica-integrated photoionization detector (SIPID) consisting of a vacuum ultraviolet (VUV) lamp, an interlayer of silica-coated VUV window, and a microfluidic channel. The VUV lamps are commercially available, which come with a 1-mm-thick built-in MgF_2 and LiF window for a Krypton (Kr) and Argon (Ar) lamp, respectively. (B) Photograph of a microfluidic chip bonded with a 10 nm-silica-coated 0.5 mm thick MgF_2 interlayer. (C) Micrograph of the center of the spiral microfluidic channel in (B). The labeled Cr and Au are on the top MgF_2 window and the bottom silicon, respectively. (D) Microfabrication process – (I) anodic bonding; (II) e-beam evaporation and lift-off; (III) deep reactive-ion etching (DRIE); (IV) plasma-enhanced chemical vapor deposition (PECVD); (V) evaporation and Au/Cr etch; (VI) Au-Au cold-welding.

For future manufacturing, the built-in VUV window on a commercial lamp can be pre-coated with silica and subsequently cold-welded to the silicon microfluidic chip without using an interlayer.

The silica coating on a VUV window may inevitably compromise the overall VUV transmission. Ideally, the silica coating should be ultrathin to minimize its VUV absorption; meanwhile, it should

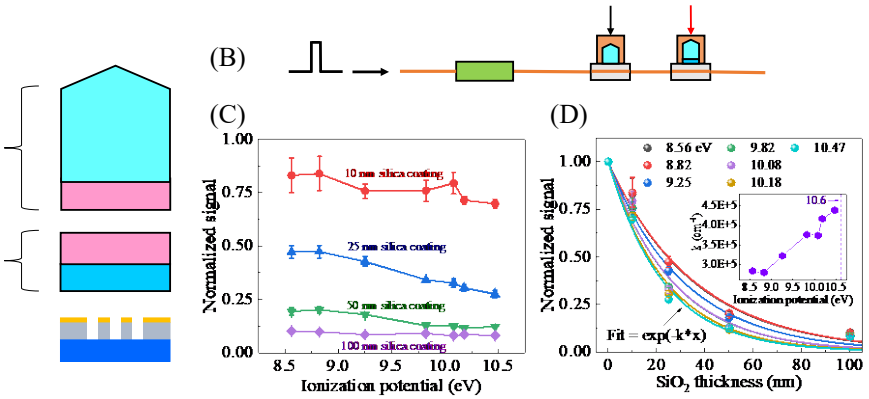

Figure 2. (A) Device structure of an SIPID using a commercial Kr lamp and a MgF_2 interlayer coated with various thicknesses (0 to 100 nm) of silica. (B) Setup used to characterize the silica VUV transmission. The analytes (see Table 1) with a range of ionization potentials (IPs) were injected via a bench-top gas chromatography (GC) injector. Two Kr-based PIDs were connected in series. The one without silica coating (*i.e.*, 0 nm silica thickness) was used to calibrate the signal obtained by the other one (*i.e.*, the device under test - DUT) coated with various thicknesses of silica. (C) Normalized signal obtained by the DUT vs. ionization potentials for different thicknesses of silica coating. The normalization is defined as the ratio of peak areas of respective analytes (with corresponding ionization potentials) between the DUT with a silica coating and the DUT having a bare interlayer without any coating. The signal of a DUT normalized to the calibration PID is presented in Figure 3. (D) Normalized signal, which reflects the overall VUV transmission efficiency of the silica coating, extracted from (C) for different silica coating thicknesses. A single exponential function (exp(-k*x)) is used to fit each curve at respective ionization potentials for extracting the corresponding pseudo-absorption coefficients. Inset: pseudo-absorption coefficient vs. ionization potential. The vertical dashed line indicates 10.6 eV. Error bars were obtained with 3 measurements.

be sufficiently thick to ensure a uniform and dense coverage on the MgF_2 or LiF window for efficiently blocking moisture permeation. To characterize the VUV transmission of the silica coating, a series of Kr lamp (10.6 eV) based SIPIDs (see Figure 2(A)) were constructed with various thicknesses of silica coating (via PECVD) on the MgF_2 interlayer. As shown in Figure 2(B), analytes (see Table 1) with a range of ionization potentials (IPs) were injected and then detected by two Kr-based PIDs connected in series. The first PID did not have an interlayer and was used to calibrate the downstream SIPIDs (i.e., the device under test - DUT) due to the non-destructive and flow-through nature of our PID.

Analyte	Ionization potential (eV)
Xylene	8.56
Toluene	8.82
Benzene	9.25
Octane (C_8)	9.82
Heptane (C_7)	10.08
Hexane (C_6)	10.18
Ethanol	10.47
Methanol*	10.85
Formaldehyde*	10.86
Dichloromethane*	11.33
Chloroform*	11.37
Carbon Tetrachloride*	11.47

Table 1. Analytes used in the experiments and their corresponding ionization potentials.

Figure 3 shows the peak area detected by the DUT normalized to that detected by the calibration PID for the analytes of different ionization potentials. The interlayers in the DUT had various silica coating thicknesses ranging from 0 nm (i.e., just a bare 0.5 mm MgF_2 window) to 100 nm. In Figure 2(C), the VUV transmission of the silica coating can be extracted by further normalizing the peak area in Figure 3 to that obtained with the 0 nm silica coating. It is found that a 10 nm silica coating retains 70-80% of the original sensitivity (i.e., 70-80% overall VUV transmission). In general, with the increased silica coating thickness, the sensitivity for the analytes with lower ionization potentials (such as IP = 8.56 and 8.82 eV) decays more slowly than for those with higher ionization potentials (such as IP = 10.18 and 10.47 eV), as shown in the inset of Figure 2(D). This can be explained as follows. First, the Kr-lamp has multiple VUV photon emission energies with the highest being 10.6 eV. The analytes with lower ionization potentials can be ionized (and subsequently detected) by not only 10.6 eV photons, but also the emitted photons with other lower energies. In contrast, the analytes with high ionization potentials (such as 10.18 and 10.47 eV) can only be ionized by 10.6 eV photons. Furthermore, silica's VUV absorption increases with increased VUV photon energy (i.e., decreased VUV photon wavelength) in the range of 8.5 – 10.5 eV. Consequently, the detection of analytes having lower ionization potentials is less impacted by the silica coating than

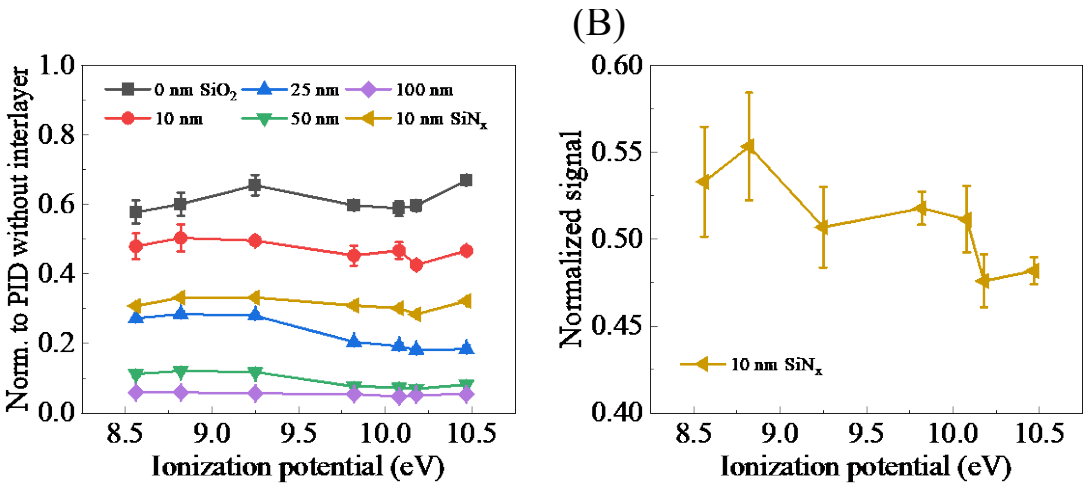

Figure 3. (A) Normalized signal of DUT with silica thickness = 0, 10, 25, 50, and 100 nm; and with 10 nm SiN_x. The normalization is defined as the ratio of peak areas of respective analytes (with corresponding ionization potentials) between the DUT and the calibration PID. (B) Normalized signal for 10 nm SiN_x vs. ionization potential. The normalization is defined as the ratio of peak areas of respective analytes (with corresponding ionization potentials) between the DUT with a 10 nm SiN_x coating and the DUT having a bare interlayer without any coating. Error bars were obtained with 3 measurements.

that of those having ionization potentials closer to 10.6 eV (see the inset in Figure 2(D)). The pseudo-absorption coefficient of the silica coating at 10.6 eV is estimated to be 4.5 x 10^5 cm^{-1} by using the decay curve of the analyte with 10.47 eV ionization potential in Figure 2(D) and a single exponential curve fit, in general agreement with the previous studies that show an absorption coefficient of 6 x 10^5 cm^{-1} at 10.6 eV for silica. Note that only the analyte whose ionization potential is close to 10.6 eV can be used to extract the silica absorption coefficient at 10.6 eV since only 10.6 eV photons can ionize it, as discussed previously.

We also explored the PECVD silicon nitride coating due to its reported better performance as a moisture barrier than silica. Only 50% of the original sensitivity was obtained for a 10 nm thick coating as shown in Figure 3(B), about 30% lower than a silica coating of the same thickness. Metallic coatings such as a thin film consisting of sputtered Cr (2.5 nm)/Au (2.5 nm) were previously reported that allowed for >50% VUV transmission on an MgF_2 window, but they have questionable moisture protection effectiveness due to the discontinuous and island-like surface typically formed by ultrathin metals. Besides, a thin metal coating is not applicable in the current μPID design as it would short the silicon electrodes of the microfluidic chip underneath.

The VUV transmission of the silica coating beyond 10.6 eV was further investigated using Ar lamps and LiF windows with a similar device structure, i.e., replacing Kr lamps (MgF_2 interlayer) with Ar lamps (LiF interlayer). Due to restrictions on processing LiF in our cleanroom facility, silica could only be sputtered on the LiF substrates instead of using PECVD. In Figure 4(A), 10 nm sputtered silica shows 40-60% of original sensitivity (i.e., overall VUV transmission) for the analytes with the ionization potential ranging from 8.5 eV to 11.5 eV. The ~20% discrepancy compared to a PECVD coating is likely caused by the extrinsic VUV transmission loss of the host LiF substrate due to its exposure to Ar plasma during the sputtering process, as evidenced by the LiF color center formation after sputtering (see Figure 4(B)).

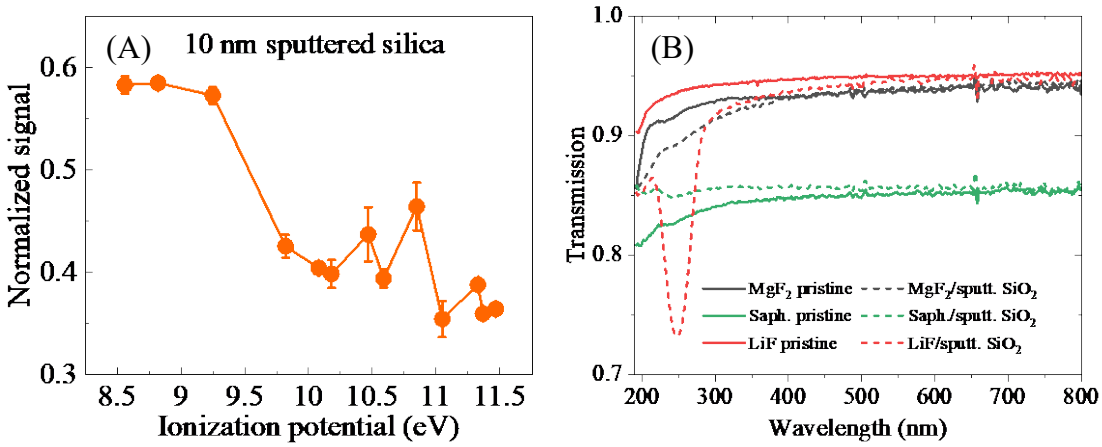

Figure 4. (A) Normalized signal for 10 nm sputtered silica vs. ionization potential. The normalization is defined as the ratio of peak areas of respective analytes (with corresponding ionization potentials) between the DUT with a 10 nm silica coating and the DUT having a bare LiF interlayer without any coating. The tested analytes are listed in Table 1. (B) Transmission spectra of pristine and silica-sputtered MgF_2, sapphire, and LiF substrates. LiF substrate developed a color center (at wavelength = 250 nm) due to exposure to Ar plasma during the sputtering process.

The reliability of PIDs was tested using the setup shown in Figure 5(A). A benchtop-GC flame ionization detector (FID) was connected downstream in series with the PID and used as the calibration detector. The relative sensitivity of the PID under test is defined as the ratio of peak areas of PID over FID. The reliability of the PID was evaluated using the time evolution of its relative sensitivity under certain aging conditions.

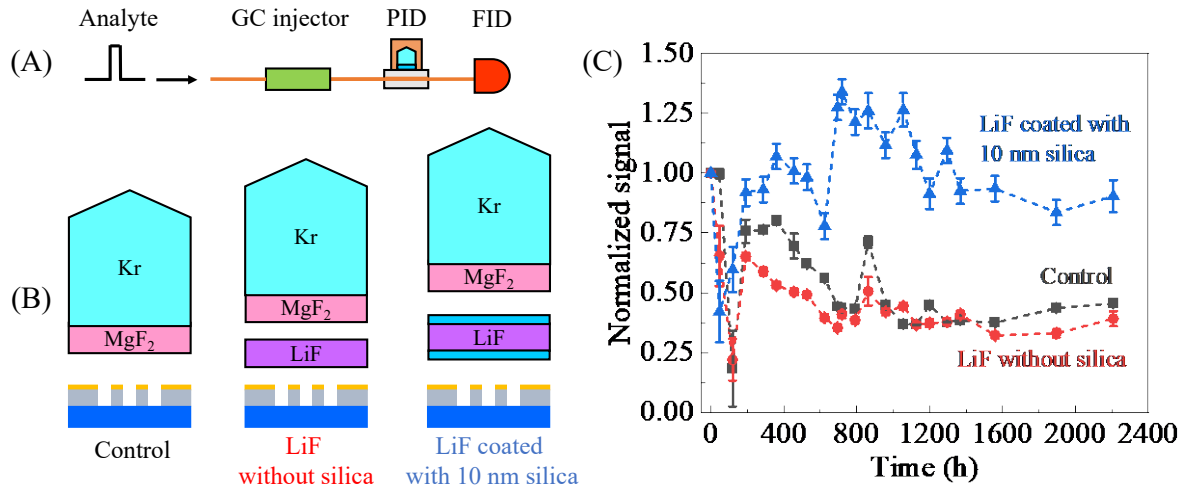

Figure 5. (A) Setup used to characterize the PID lifetime. A flame ionization detector (FID), assumed to have no degradation, was fluidically connected to the SIPID as the calibration detector. (B) Kr lamp based PIDs for lifetime test – (1) control PID without any interlayer (i.e., the Kr lamp was directly placed and sealed on the top of the microfluidic chip); (2) PID with a bare LiF interlayer; (3) PID with a LiF interlayer coated with 10 nm silica on both sides. Note that only the bottom surface of the interlayer was exposed to microfluidic channels and hence the ambient environment. The top surface was sealed by surrounding UV-epoxy, which is assumed to have no water vapor coming from outside. (C) Signal over aging time obtained by the three devices in (B). The signals from each device are normalized to its relative sensitivity (i.e., PID/FID) at the 0th hour. The PIDs were aged in ambient with a temperature of 19.7±0.7 °C and relative humidity of 41.5±10.4%. The signal of the PIDs was periodically measured using benzene (IP = 9.2 eV). The Kr lamps and the FID were turned off without carrier gas during aging intervals. Error bars were obtained with 3 measurements.

To examine the silica protection performance on VUV windows against moisture, we designed a hybrid device architecture of SIPID – in which the more hygroscopic LiF window (with or without silica) was selected as the interlayer exposed to ambient to amplify the moisture effect (since MgF_2 window is less susceptible to moisture); and the Kr lamp was employed as the VUV source due to its known superior robustness to an Ar lamp. Therefore, other possible degradation mechanisms associated with an Ar lamp (see the discussion later) could be ruled out and the VUV light source was deemed stable throughout the test. As shown in Figure 5(B), two SIPIDs (one with a bare LiF interlayer and the other with a 10 nm silica double-coated LiF interlayer) and a control device without interlayer were tested. Note that the 10 nm silica coating on the top LiF interlayer surface was for precaution only, which was essentially unnecessary as its perimeter was sealed by UV-epoxy that has a very low water vapor transmission rate. The PIDs were aged in ambient with a temperature of 19.7±0.7 °C and a relative humidity of 41.5±10.4%, which translates to a dew point = 8.0±1.8 °C. This dew point is close to the annual average value recorded at Detroit Metro Airport station in Michigan. The signal (i.e., relative sensitivity) of the PIDs was periodically measured using benzene (IP = 9.2 eV). Between two consecutive measurements (i.e., during an aging cycle), the PIDs were not in operation with the Kr lamp (i.e., plasma) and carrier gas being turned off.

Figure 5(C) shows the moisture reliability of the three devices. The silica-coated LiF device maintained its sensitivity at 90% after 2,200 hours of aging. In comparison, both the control device and bare LiF device have degraded to 45% and 39%, respectively, with the same aging time. We observed that the bare LiF device underwent the fastest degradation among the three devices in the first 800 hours, after which the sensitivity plateaued at ~40%. The control device (i.e., the one with a built-in MgF_2 window only) shared a similar trend reaching the 40% plateau with a slower degradation rate. The results suggest that the LiF window experiences faster degradation when exposed to ambient than the MgF_2 window (control), while the eventual VUV transmission loss after a long term is similar for both windows. In contrast, the silica-coated LiF window (or interlayer) shows no obvious degradation trend with only 10% VUV loss when sensitivity plateaued, attesting

to the effective moisture protection of the 10 nm silica coating for VUV windows.

We next implement the ultrathin silica integration to the LiF interlayers in the Ar lamp based SIPIDs (Ar-SIPID), as shown in the inset of Figure 6, to examine whether Ar lamp lifetime could be improved. Figure 6(A) demonstrates the moisture reliability test of control and silica-coated Ar-SIPIDs. The aging protocol was the same as previously described in Figure 5. Surprisingly, both devices degraded almost identically over 700 hours of aging regardless of silica protection. Compared to the results using the Kr lamps in Figure 5, Ar-SIPIDs' sensitivity had a faster degradation rate without plateauing. In addition, it was visually observed that the built-in LiF windows in both Ar lamps of the tested Ar-SIPIDs appeared yellowish just after ~50 hours of aging, and such yellowish discoloration was manifested throughout the whole bulk crystal of LiF. All evidence suggests that there are new degradation mechanisms in the Ar lamp itself that are faster than the moisture-induced degradation discussed previously.

The major new degradation source turns out to be the Ar plasma generated inside the Ar lamp. To decouple its impact from the moisture reliability test performed before, another control device (i.e., Ar-SIPID without silica) was constructed and it was aged with Ar plasma being turned on continuously. As evidenced in Figure 6(B), with constant Ar plasma aging, the Ar-SIPID demonstrated an accelerated exponential-like decay, taking only 2 hours to drop to 75% and 30% for benzene (IP = 9.2 eV and dichloromethane (DCM, IP = 11.3 eV), respectively. In addition, the yellowish discoloration of the built-in LiF window has also developed (not necessarily requiring 2 hours). Such results indicate that the dominant aging of Ar-SIPIDs in Figure 6(A) could be

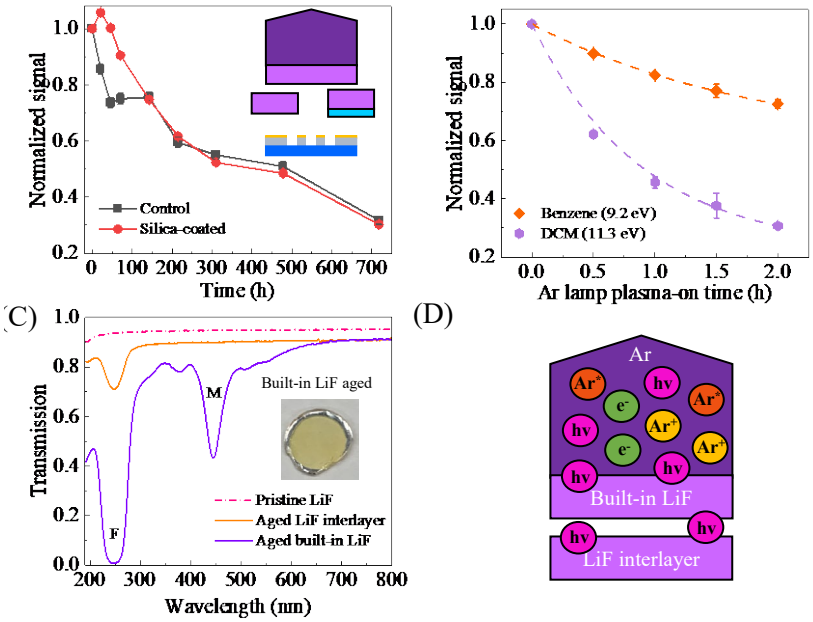

Figure 6. (A) Signal of Ar-SIPIDs (with and without silica) for heptane (IP = 10.1 eV) vs. time. The signals from each device are normalized to its relative sensitivity at the 0th hour. Inset: Ar lamp based SIPIDs (Ar-SIPID) with (1) bare LiF interlayer as a control and (2) silica-coated (10 nm) LiF interlayer. The aging protocol was the same as in Figure 5(C) that the plasma was only turned on during each measurement point. (B) Normalized signal of another Ar-SIPID in continuous operation (i.e., the Ar lamp was turned on throughout the aging experiment) vs. aging time for benzene (IP = 9.2 eV) and dichloromethane (DCM, IP = 11.3 eV). Dash lines are the fitting curves of a single exponential decay function (A*exp(-k*x)+C). The exponential decay constants are k = 0.53 h-1 and 1.14 h-1 for benzene and DCM, respectively. A and C are fitting constants. (C) Transmission spectra of pristine LiF, aged interlayer LiF, and aged built-in LiF. F and M refer to the F color center and M color center, respectively. The aged interlayer and the built-in LiFs were dissembled from the 700-hour aged control Ar-SIPID (i.e., without silica). The inset shows a photo of the dissembled aged built-in LiF window. (D) Conceptual illustration of different degradation agents generated by Argon plasma and their exposure to built-in and interlayer LiF windows – (1) Ar*: Argon excited state; (2) Ar+: Argon ion; (3) e-: electron; (4) hv: VUV photon.

attributed to the accumulated short-term (approximately 30 minutes) Ar plasma exposure when it was turned on during the measurements at each aging test time point. Additionally, throughout 700 hours of moisture aging, the sensitivity loss for DCM is faster than toluene (IP = 8.8 eV) and heptane (10.1 eV, Figure 6(A)), consistent with the trend observed in Figure 6(B) with accelerated Ar plasma exposure, that is, the sensitivity decays faster for the analytes whose ionization potentials are closer to the maximum emitted photon energy of Ar plasma (11.7 eV), as discussed in Figure 2(D) for the Kr plasma case.

To better understand the degradation mechanism of the LiF windows in the Ar-SIPID, the built-in LiF window as well as the interlayer LiF window were dissembled from the 700-hour aged control Ar-SIPID (i.e., without silica) for further characterizations. From the transmission spectra in Figure 6(C), the aged built-in LiF window shows two dominant signature color centers of LiF (labeled as F and M), which render its yellowish appearance as seen in the inset of Figure 6(C). These color center formations result from high energy irradiations (e.g., X-rays, Extreme UV (EUV), VUV, heavy ions, protons, electrons, etc.). Opposite to the significantly deteriorated built-in LiF window, the directly contacted LiF interlayer underneath only developed a small F center without any visual discoloration, indicative of different degradation mechanisms. As illustrated in Figure 6(D), the built-in LiF window was directly exposed to all four species generated by Ar plasma inside the lamp body - (1) Ar*: Argon excited state; (2) Ar+: Argon ion; (3) e-: electron; and (4) hv: VUV photon (e.g., 11.7 eV). In contrast, the LiF interlayer was only subject to the VUV photons transmitted through the built-in window. The above comparison suggests that the combination of Ar excited states, Ar ions, and electrons might play a more detrimental role to the LiF than VUV photons. However, it is also worth noting that the dose of VUV photons (hence the damage) incident on the LiF interlayer is lower than that on the native built-in LiF window during aging, especially after the built-in window became yellowish. Indeed, a similar effect was observed previously when a VUV-transmissive indium thin film was coated on the LiF substrate exposed to Ar discharge. It was found that the ratios of the initial slopes of the decay curves (i.e., VUV transmission of the LiF) closely matched the ratios of the initially transmitted intensities determined by the thickness of the indium thin film.

The fact that the LiF interlayer suffered only mild degradation from Ar plasma with the shielding of the built-in window described in the previous section suggests a rational design to eventually integrate an ultrathin dielectric (e.g., silica) coating on the inner surface of the built-in LiF window in an Ar lamp as depicted in Figure 7(A). Unlike vulnerable LiF, silica is not susceptible to any color center formation and has one of the lowest sputtering yields of any standard materials when exposed to Ar plasma (meaning that silica can withstand Ar plasma very well). Combined with its decent transmission in VUV as described before, ultrathin silica becomes a promising candidate to protect LiF from Ar plasma.

Limited by the incapability to build an actual Ar lamp in-house, we performed Ar plasma aging on the bare and silica-coated LiF substrates using a commercial Ar plasma chamber, which simulated the actual environment inside an Ar lamp as illustrated in Figure 7(A). After aging in the plasma chamber, the LiF substrates were inserted as an additional interlayer into a Kr lamp based PID device, as illustrated in Figure 7(B), to extract the VUV transmission loss. Once again, we used a Kr lamp (instead of an Ar lamp) to provide a stable VUV source, as discussed previously. In addition, a stretchable tape instead of UV-epoxy was used for easy removal of the assembled VUV lamp and the interlayer between two consecutive aging cycles. The overall VUV transmission loss is hence inferred as the said PID sensitivity loss, assuming that other components in the stack (i.e., the Kr lamp and MgF_2 interlayer) stayed intact.

In Figure 7(C), the 10 nm silica-coated LiF substrate remained stable (with a 15% increase in fact) after 11.5 hours of exposure to Ar plasma. In contrast, the bare LiF decreased to 60% of its original VUV transmission for the same aging. Figures 7(D)-(F) present the UV-VIS spectra obtained simultaneously with another batch of substrates, showing that bare LiF progressively developed the F and M color centers with overall transmission loss, resulting in visual

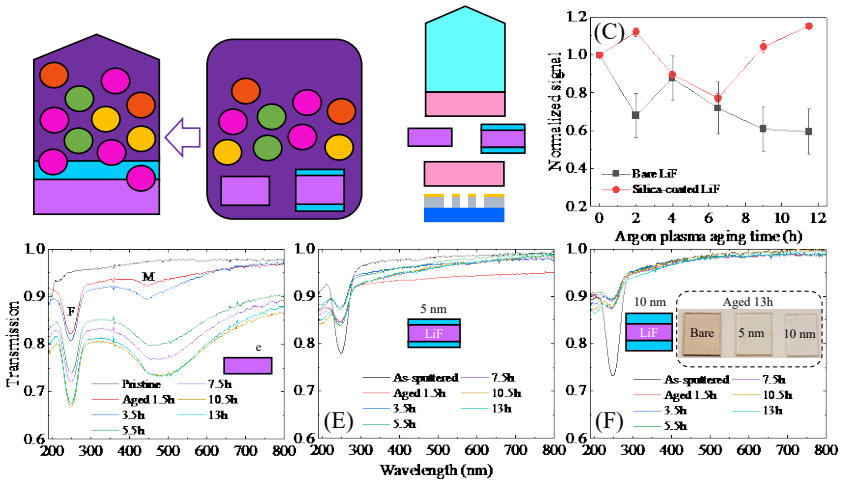

Figure 7. (A) Simulating Ar plasma aging. (Left) Conceptual design of an Ar lamp with silica coating on built-in LiF facing inward. (Right) The aging effects in an Argon-lamp setting illustrated on the left were simulated by placing (1) bare and (2) silica-coated LiF interlayers inside an Argon plasma chamber. (B) Device structure for testing VUV degradation of bare and silica-coated LiF interlayers after they were aged in an Argon plasma chamber in (A). During the test, a stretchable tape was used to sandwich the LiF interlayer between the Argon lamp and the microfluidic chip. After each test, the LiF interlayer was disassembled and placed back in the Argon plasma chamber for further aging. (C) Normalized signal of the device in (B) with respect to the argon plasma aging time for both bare and silica-coated LiF interlayer (10 nm coated on both sides) using benzene (IP = 9.2 eV) as the analyte. The signal is normalized to the relative sensitivity obtained at the 0th hour for each interlayer. The testing protocol is the same as shown in Figure 5. Error bars were obtained with 3 measurements. (D) – (F) Transmission spectra of a bare and silica-coated LiF (5 nm and 10 nm on both sides) interlayer at different Ar plasma aging times. Inset in (F) shows the photos of aged samples of bare, 5 nm silica-coated, and 10 nm silica-coated LiF. F and M in (D) refer to the F color center and the M color center, respectively.

discoloration after 13 hours of aging (see the inset in Figure 7(F)). In contrast, the silica-coated LiF substrates showed an initial F color center as-sputtered, which in fact partially recovered after the first 1.5 hours of aging, and the overall transmission stayed relatively stable without developing any other new color centers. Compared to small fluctuations in the transmission spectra of the 5 nm silica-coated LiF substrate, the 10 nm sample presents an almost constant overall transmission during aging. As mentioned before, the initial F color center of the silica-coated samples is caused by the sputtering process using Ar plasma, as further evidenced by the lower transmission value of the F center (at wavelength of 250 nm) in 10 nm coating (0.73) than that of 5 nm (0.78). It is worth noting that the phenomenon of an initial partial recovery of the F center is consistent with the small increase of the VUV transmission observed in Figure 7(C), which also occurred right after the first 2 hours of aging. Such healing of the color center can likely be explained as the UV bleaching effect by the UV photons generated inside the Ar plasma chamber.

The above proof-of-concept experiments using an Ar plasma chamber suggest that ultrathin silica can effectively prevent VUV transmission loss of and color center formation in LiF from Ar plasma exposure and thus can potentially be integrated on the inner surface (i.e., facing plasma) of a LiF (and MgF_2) window to increase the Ar (and Kr) lamp lifetime. In contrast, other VUV transmissive thin films, such as the aforementioned indium or gold, are not applicable, because their metallic nature would disrupt the dielectric environment for dielectric-barrier-discharge (DBD) plasma to form inside a VUV lamp.

2. System level: Portable Comprehensive Two Dimensional Micro-Gas Chromatography Using Integrated Flow-Restricted Pneumatic Modulator

Two dimensional (2D) gas chromatography (GC) provides enhanced vapor separation capabilities compared to conventional one dimensional GC and is useful for the analysis of highly complex chemical samples. We developed a microfabricated flow-restricted pneumatic modulator (FRPM) for portable comprehensive 2D micro-GC (μGC), which enables rapid ^{2}D injection and separation without compromising ^{1}D separation speed and eluent peak profiles. ^{2}D injection characteristics such as injection peak width and peak height were fully characterized by using flow-through micro-photoionization detectors (μPIDs) at the FRPM inlet and outlet. A ^{2}D injection peak width of ~25 milliseconds can be achieved with a ^{2}D/^{1}D flow rate ratio over 10. The FRPM was further integrated with a 0.5 m long ^{2}D μcolumn on the same chip and its performance was characterized. Finally, we developed an automated portable comprehensive 2D μGC consisting of a 10 m OV-1 ^{1}D μcolumn, an integrated FRPM with a built-in 0.5 m polyethylene glycol (PEG) ^{2}D μcolumn, and two μPIDs. Rapid separation of 40 volatile organic compounds in ~5 minutes was demonstrated. A 2D contour plot was constructed by using both ^{1}D and ^{2}D chromatograms obtained with the two μPIDs at the end of the ^{1}D and ^{2}D μcolumns, which was enabled by the presence of the flow resistor in the FRPM.

A block diagram for the FRPM along with its operation is provided in Figure 8. The FRPM consists of an inlet for auxiliary flow (Port 1), an inlet for ^{1}D eluents (Port 2), an outlet connected to the ^{2}D column (Port 3), and an outlet as the waste line (Port 4), as well as an internal flow resistor between ^{1}D and ^{2}D. The auxiliary flow and waste line are controlled by two 2-port valves. During loading (Figure 8(A)), both valves are closed and a portion of the ^{1}D eluent is loaded onto the ^{2}D column through the flow resistor. During ^{2}D separation (Figure 8(B)), both valves are open, and a high auxiliary flow simultaneously provides the ^{2}D carrier gas flow for ^{2}D separation and the buffer flow that prevents the ^{1}D eluent from entering the ^{2}D column. Concurrently, ^{1}D separation continues and the ^{1}D eluent is diverted to the waste line. After ^{2}D separation, both valves are

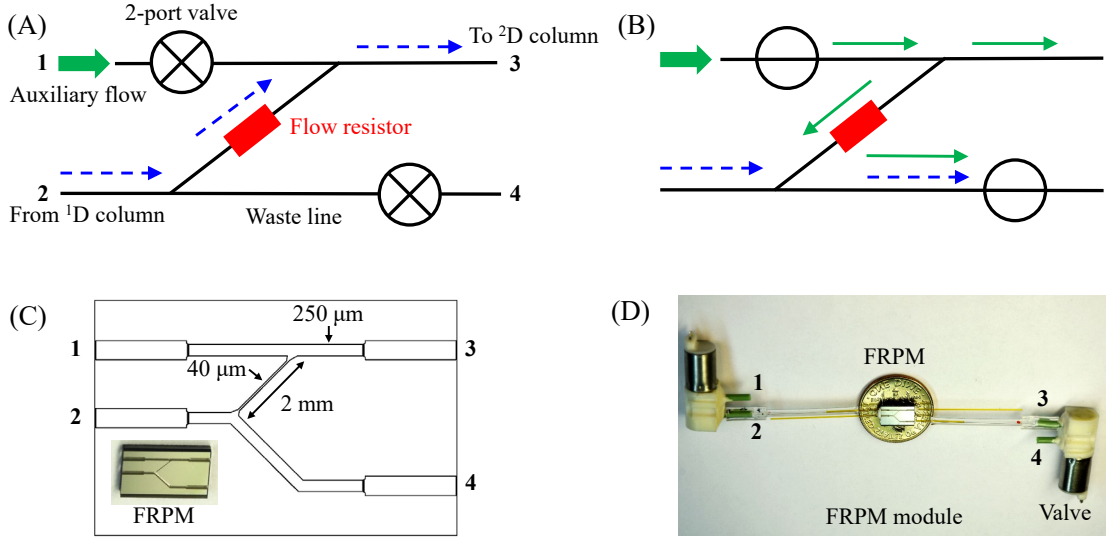

Figure 8. Flow-restricted pneumatic modulator (FRPM) operation for comprehensive 2D μGC. (A) ^{1}D to ^{2}D loading configuration with both valves closed (typical flow rate: ~1 mL/min). The blue arrows depict the ^{1}D flow direction. (B) ^{2}D separation with both valves open for high ^{2}D flow (typical flow rate: ~10 mL/min), enabling sharp ^{2}D injection and rapid ^{2}D separation. The green arrows depict the auxiliary flow direction. (C) Microfabricated FRPM schematic and photograph. The flow resistor is a narrow channel with a cross section of 40 μm x 170 μm (width x depth) and a length of 2 mm. All other channels had cross sections of 250 μm x 250 μm (width x depth). (D) Photograph of the FRPM module with FRPM and two 2-port valves. Ports 1-4 are labelled on the schematics and photographs.

closed again, and a new modulation cycle begins.

FRPM chips were microfabricated using the nanofabrication facilities at the University of Michigan. Each FRPM chip had dimensions 8 mm x 5 mm x 1 mm (length x width x thickness). Figure 8(C) illustrates the schematic of the microfluidic channels inside the FRPM, with a 2 mm long, 40 µm x 170 µm (width x depth) channel as the built-in flow resistor. The flow resistor's width and depth can be adjusted to achieve different flow resistances. All other channels had cross sections of 250 µm x 250 µm. FRPM modules were constructed by connecting the FRPM chip to two 2-port valves at the corresponding ports (Figure 8(D)).

As illustrated in Figure 9(A), ^{2}D injection using the FRPM module was characterized with only a 10 m OV-1 ^{1}D µcolumn and a 20 cm guard column in ^{2}D (no ^{2}D separation column). Two flow-through µPIDs were used to measure and compare eluents right before and after the FRPM. Initial characterization was carried out using unmodulated operation. All ^{1}D eluents were transferred to ^{2}D with slight delays between the eluent peaks detected by the ^{1}D and ^{2}D µPID, which increased for heavier compounds. These delays resulted from the 20 cm guard column in ^{2}D. Comparison of the C_6 and C_7 peak height showed that the ^{2}D µPID is about 2.4 times more sensitive than the ^{1}D µPID. Relative peak heights for other compounds were reduced in the ^{2}D µPID as compared to ^{1}D again due to peak broadening resulting from the 20 cm guard column.

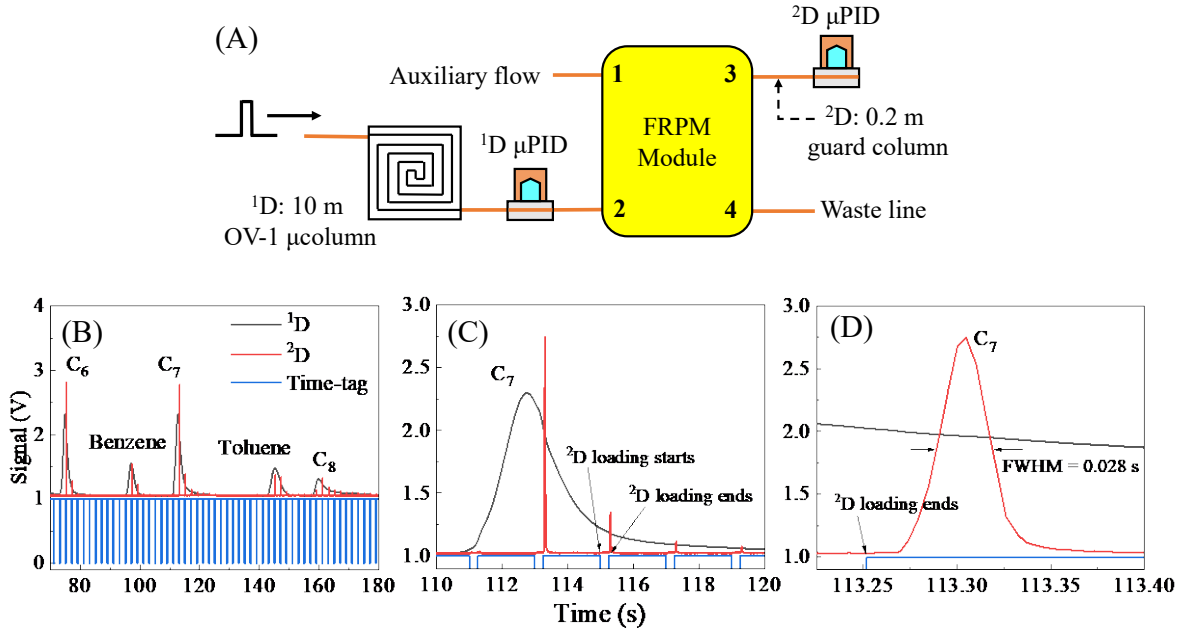

Figure 9. (A) Setup used to characterize the FRPM module. The sample mixture was injected into a 10 m OV-1 coated microcolumn (µcolumn) with cross sections of 200 µm x 250 µm (width x depth). A microphotoionization detector (^{1}D µPID) was connected to the ^{1}D µcolumn and monitored the ^{1}D eluents. The ^{2}D µPID was connected to the outlet of the FRPM module via a 20 cm guard column (inner diameter: 250 µm) and monitored the ^{2}D eluents. Ports 1-4 labelled on the FRPM module are described in Figure 8(A). (B) ^{1}D and ^{2}D chromatograms of C_6, C_7, C_8, benzene, and toluene. The time-tags (shown as blue square wave) record the closed (= 0) and open (= 1) states of the FRPM module valves, corresponding to ^{2}D loading (= 0) and ^{2}D separation (= 1), respectively. (C) Zoom-in of C_7 in ^{1}D and ^{2}D. (D) Zoom-in of C_7 in ^{2}D. Experimental conditions: loading time = 0.25 s; modulation time = 2 s; ^{1}D flow rate = 1.2 mL/min (measured at Port 3 with both valves closed). The flow rate was nearly the same when measured at the outlet of ^{1}D (before the FRPM), indicating that the impact of the flow resistor on the ^{1}D flow is negligible. ^{2}D flow rate = 20 mL/min (measured at Port 3 with both valves open). The FRPM was kept at isothermal ambient temperature (~20 °C). Helium was used as both ^{1}D carrier gas and auxiliary flow.

Modulated operation was investigated next. Figures 9(B)-(D) show an example of ^{1}D and modulated ^{2}D chromatograms using alkanes and aromatics. The heights of the modulated ^{2}D peaks are lower than that for the unmodulated ones, because the loading from ^{1}D to ^{2}D may not

occur exactly at the apexes of the ^{1}D peaks. Since sharp ^{2}D injections are crucial for maximizing ^{2}D peak capacity, the ^{2}D injection peak width (defined as the full-width-at-half-maximum) for C_6, C_7, and C_8 as a function of the flow rate ratio between ^{2}D and ^{1}D (^{2}D/^{1}D) was examined (Figure 10(A)). In general, the injection peak width decreases with increased ^{2}D/^{1}D flow rate ratio. However, the measured injection peak width is always broader than the ideal peak width (defined as the loading time divided by ^{2}D/^{1}D flow rate ratio). This broadening is caused by the 20 cm guard column and the broadening vs. flow rate can be viewed as the Golay plot of said column (Figure 10(B)). The ^{2}D injection peak width is also affected by loading time and is characterized in Figure 10(C) at a fixed flow rate ratio of 13. The measured peak width increases linearly with increased loading time and is again broader than the theoretical value. The broadening effect diminishes with longer loading times (Figure 10(D)) since the broadening from the guard column becomes less prominent. In addition, we also experimentally tested a series of flow resistors with widths of 20, 60, 80, and 250 μm. Considering an appropriately high flow rate ratio of ~10, ^{1}D flow jittering was only eliminated once the flow resistor's width was reduced to 40 μm (depth = 170 μm). A width of 20 μm also eliminated the ^{1}D jittering but was prone to channel blocking during microfabrication. Based on these results, we selected the FRPM chip with a flow resistor width x depth = 40 μm x 170 μm, which allowed for an injection peak as sharp as ~25 ms achieved with a loading time of 0.25 s and a flow rate ratio larger than 10. This was accomplished without perturbing the ^{1}D flow or significantly slowing down ^{1}D separation due to the sufficiently high flow resistance of the 40 μm channel.

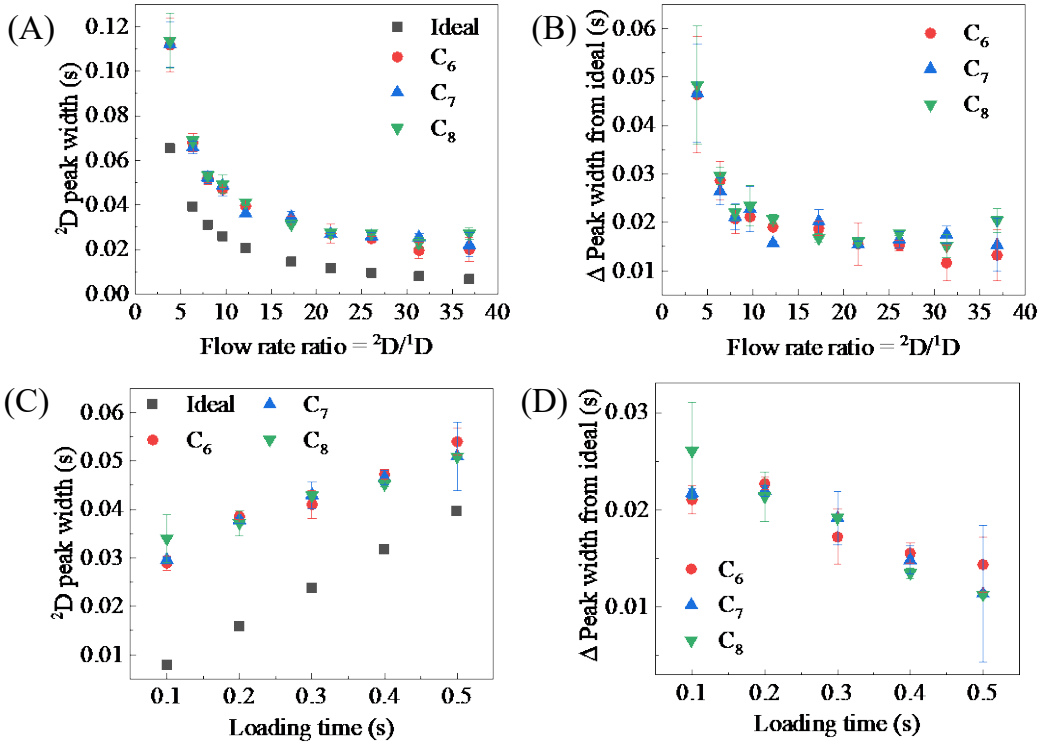

Figure 10. ^{2}D peak widths (full width at half maximum) of C_6, C_7, and C_8 detected by ^{2}D μPID vs. ^{2}D/^{1}D flow rate ratio (A) and loading time (C). The ideal ^{2}D peak width is calculated by the loading time divided by the flow rate ratio. Deviations of ^{2}D peak widths from ideal injection widths vs. flow rate ratio (B) and loading time (D). In (A) and (B), the loading time was fixed at 0.25 s and the ^{2}D flow rate varied from 4 to 40 mL/min. In (C) and (D), the ^{2}D flow rate was fixed at 16 mL/min and the loading time varied from 0.1 to 0.5 s. In all experiments, ^{1}D flow rate = 1.2 mL/min and modulation time = 2 s. Error bars are obtained with 3 measurements.

To further reduce the device footprint and number of interconnections, the FRPM was integrated with a 0.5 m ^{2}D µcolumn (cross section: 250 µm x 250 µm) on a single chip of dimensions 18 mm x 15 mm x 1 mm (length x width x thickness) (Figures 11(A) and (B)). Because of the additional flow resistance from the 0.5 m ^{2}D µcolumn, the integrated module was re-evaluated with the same methodology as the stand-alone module. As shown in Figures 11(C)-(E), at a flow rate ratio = 13, the integrated FRPM module demonstrated similar performance to the stand-alone module with an additional ^{2}D peak broadening of ~20 ms due to the extra 0.5 m µcolumn (the ^{2}D µcolumn was only deactivated without any stationary phase coating yet).

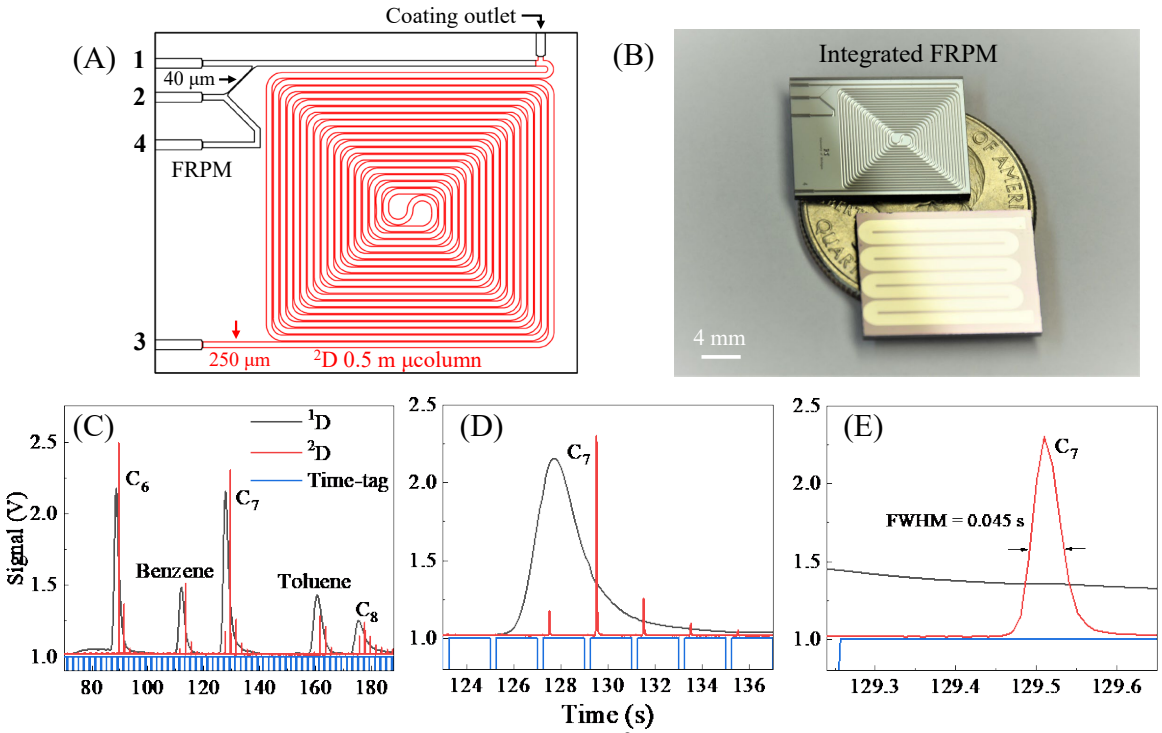

Figure 11. (A) Schematic of FRPM integrated with 0.5 m ^{2}D µcolumn. (B) Photograph of integrated FRPM chip (top) with backside heater (bottom). (C) ^{1}D and ^{2}D chromatograms of C_6, C_7, C_8, benzene, and toluene using deactivated integrated FRPM chip. (D) Zoom-in of C_7 in ^{1}D and ^{2}D . (E) Zoom-in of C_7 in ^{2}D. Experimental conditions: loading time = 0.25 s; modulation time = 2 s; ^{1}D flow rate = 1.1 mL/min; ^{2}D flow rate = 14 mL/min. The ^{1}D temperature ramping profile was the same as in Figure 3. The integrated chip was at isothermal room temperature (~20 °C). Helium was used as both ^{1}D carrier gas and auxiliary flow.

We constructed a stand-alone automated portable comprehensive 2D µGC device (Figure 12) consisting of a 10 m OV-1 ^{1}D µcolumn (non-polar), the integrated FRPM and 0.5 m WAX ^{2}D µcolumn (polar), and two flow-through µPIDs at the ^{1}D and ^{2}D outlets, respectively, as well as accessories such as valves, pre-concentrator, pump, helium cartridges, and in-house control software. Miniaturized comprehensive 2D GC at the sub-system level was investigated previously using µcolumns and thermal/pneumatic modulators. However, these devices used benchtop GC injectors and/or detectors and were thus not automated stand-alone systems for field applications. This work presents a first-in-kind automated portable comprehensive 2D µGC without using any benchtop components.

This comprehensive 2D µGC is different from traditional comprehensive 2D GC in a few aspects. First, traditional comprehensive ^{2}D GC uses only one detector at the end of the ^{2}D column. The ^{1}D chromatogram is reconstructed only based on information from the ^{2}D detector, which leads to errors in ^{1}D retention time, ^{1}D peak broadening, and possibility of under-sampling of ^{1}D peaks. In contrast, our comprehensive 2D µGC uses two flow-through µPIDs to monitor the

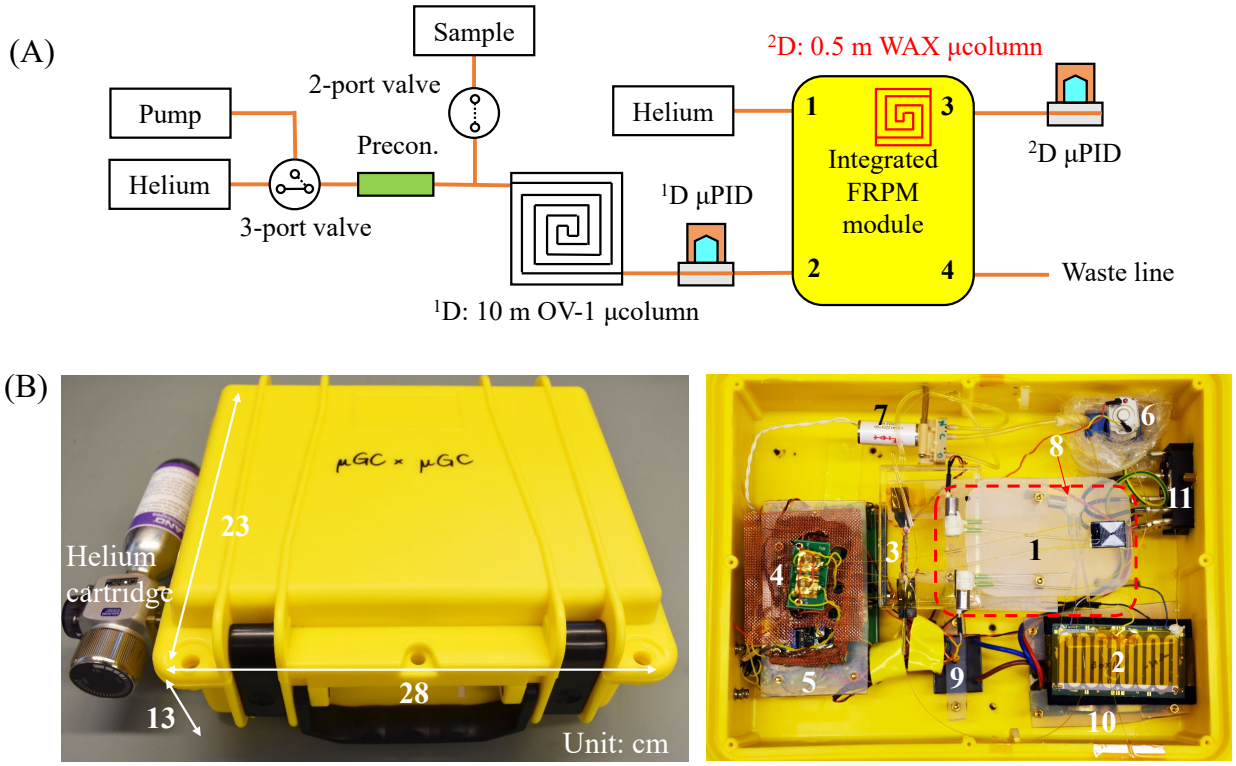

Figure 12. (A) Schematic of the integrated FRPM-based portable comprehensive 2D µGC device. The integrated FRPM module contains a 0.5 m long WAX ^{2}D µcolumn. (B) System photographs. The device has dimensions 28 cm x 23 cm x 13 cm (length x width x height) and weighs 2.4 kg (including helium cartridge). 1. Integrated FRPM and 0.5 m WAX ^{2}D µcolumn module (within the dashed square); 2. ^{1}D 10 m OV-1 µcolumn; 3. Preconcentrator. 4. µPID array; 5. Printed circuit board and data acquisition card (copper mesh shielded); 6. Pump; 7. 3-port valve; 8. 2-port valve; 9. DC-DC converter; 10. 24 V power supply; 11. Rocker switch connected to wall power.

^{1}D and ^{2}D eluents. This arrangement removes the need for ^{1}D chromatogram reconstruction, as the ^{1}D chromatogram can directly be obtained from the ^{1}D µPID. As a result, the ^{1}D peak position (*i.e.*, ^{1}D retention time) is accurately determined and the original ^{1}D peak width is preserved, which improves the separation performance (*i.e.*, peak capacity). Second, because of the two-detector arrangement, a new algorithm to generate 2D contour plots could be developed to improve the separation performance. Third, the modulation time is dynamically adjusted to accommodate different ^{1}D peak widths. For example, a short modulation time was used for earlier eluents with sharper peak widths—which reduces the chance for under-sampling—and a longer modulation time for later eluents to accommodate the generally broader ^{2}D peaks that require longer analysis times for separation.

The comprehensive 2D µGC device was employed to separate 40 VOCs (selected such that some have similar boiling points but different polarities to enable ^{2}D separation) in ~5 minutes in Figure 13. The ^{2}D column (*i.e.*, the integrated FRPM module) was operated using a carefully tuned temperature profile in order to balance the sharpness of the ^{2}D elution peaks while maintaining sufficient ^{2}D separation. Figure 13(A) shows the ^{1}D and modulated ^{2}D chromatograms obtained by the ^{1}D and ^{2}D µPIDs, respectively. Two zoom-ins are provided to visualize exemplary additional separations in ^{2}D (Figures 13(B)-(E)). For example, in Figures 13(B) and (C), two VOCs were completely co-eluted in ^{1}D yet separated in ^{2}D. Figure 13(F) presents the 2D contour plot generated using both ^{1}D and ^{2}D chromatograms obtained (see Methods for brief description of the new contour plot method). Throughout the entire analysis, each analyte was eluted from the ^{2}D column within a single modulation cycle, *i.e.*, no wrap-around was observed. By virtue of the additional ^{1}D information, more peaks are identified in the same segment (*e.g.*, Figure 13(G) and

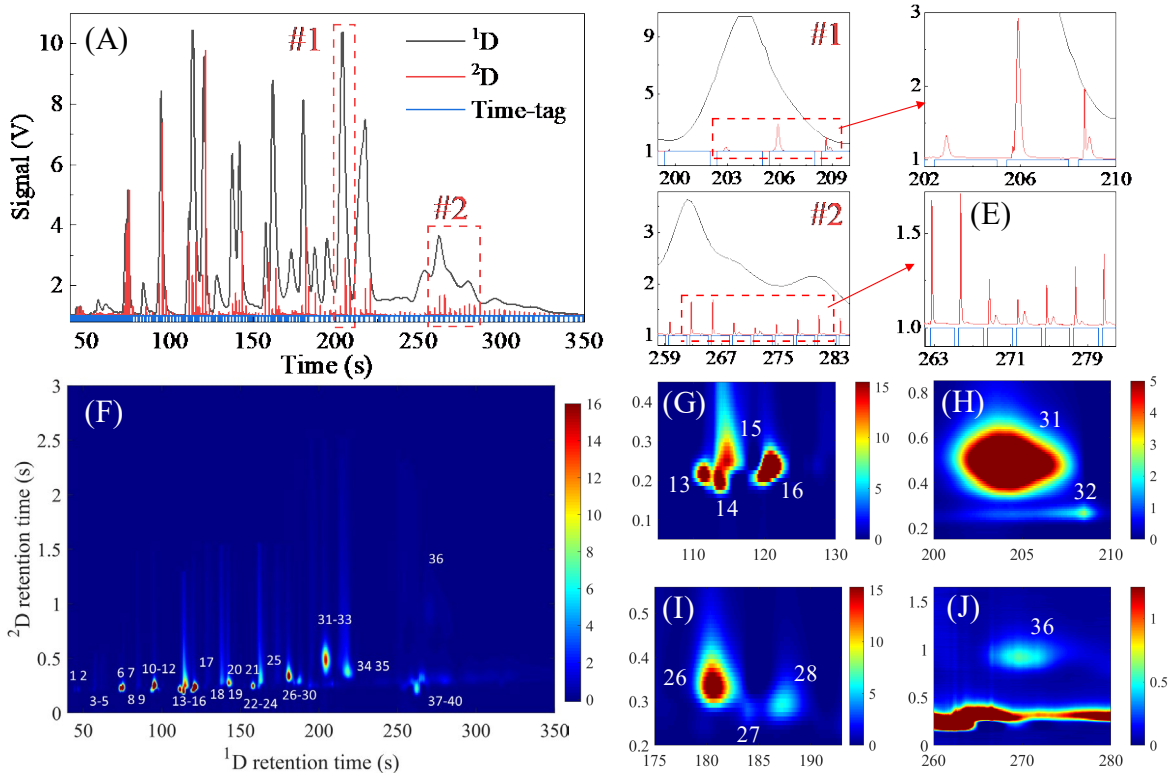

Figure 13. (A) ^{1}D and ^{2}D chromatograms of 40 VOC mix obtained by ^{1}D and ^{2}D μPIDs in the portable comprehensive 2D μGC device. Zoom-in of area #1 (B, C) and area #2 (D, E) in ^{1}D and ^{2}D. (F) 2D contour plot using the new method that relies on both ^{1}D and ^{2}D chromotograms in Figure (A). Zoom-in of peaks 13-16 (G), 31-32 (H), 26-28 (I) and 36 (J). Figures (H) and (J) correspond to (C) and (E) respectively. For comparison, the 2D contour plot using the conventional method that relies only on the ^{2}D μPID data is presented in Figure S18. Experimental conditions: ^{1}D flow rate = 1.2 mL/min; ^{2}D flow rate = 11 mL/min. Loading time = 0.4 s; modulation was segmented into three periods: modulation time = 1 s from 0 to 75 s; 2 s from 75 to 180 s; and 4 s from 180 to 350 s. Both ^{1}D μcolumn (OV-1) and ^{2}D integrated FRPM module underwent temperature ramping. Helium was used as both ^{1}D carrier gas and auxiliary flow.

(I)) compared to the conventional 2D contour plot. As a result, all 40 VOCs are separated using our new method vs. only 32 peaks using the conventional 2D contour plot method.

In order to pursue further miniaturization, we recently developed and constructed an automated battery-powered μGC device (see Figure 14) with unprecedented size (0.88 L), weight (900 g), including 0.34 L and 450 g from the battery box.

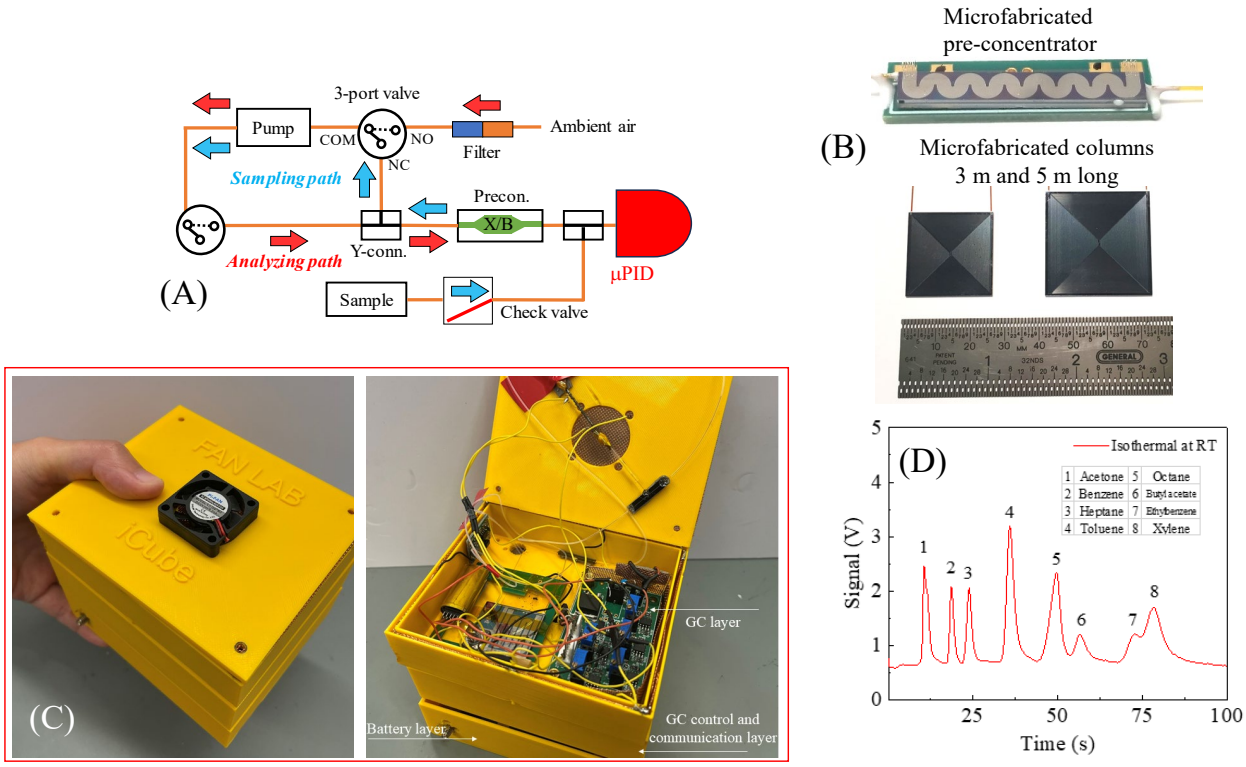

Figure 14. (A) Layout of the proposed micro-GC-AGID. (B) Microfabricated pre-concentrator and columns. A heater can be microfabricated at the back of the pre-concentrator and column for rapid injection and column temperature ramping. (C) Preliminary micro-GC device built in the Fan lab. It follows the layout in (A) but uses a regular PID as the detector that will be replaced by the proposed AGID. The device uses a 3-m long micro-column and dry/clean air as the carrier gas. It is powered by batteries. The total volume and the weight of the device are 0.88 L and 900 g, respectively, including 0.34 L and 450 g from the battery box. (D) Example of rapid separation of 8 gas analytes in 80 s isothermally at room temperature using the device shown in (C) – with a regular PID as the detector.

3. Algorithm development: Differential Calibration of Contour Plot Using 1D Data in Comprehensive Two-Dimensional Gas Chromatography

Comprehensive two-dimensional gas chromatography (GC×GC, see Figure 15(A)) uses two columns of different stationary phases so that vapor analytes are subjected to two independent separations to achieve a peak capacity higher than the corresponding one-dimensional GC. A modulator is placed between the ^{1}D and ^{2}D columns and periodically sends a portion of the ^{1}D eluent to the ^{2}D column. Usually, a thermal modulator or pneumatic modulator are used to achieve so-called snapshot modulation and accumulative modulation, respectively.

In a conventional GC×GC (Figure 15(A)), only a ^{2}D detector is used at the end of the ^{2}D column to detect the eluents coming out of the ^{2}D column. A two-dimensional (2D) chromatogram is constructed by using the ^{2}D chromatograms directly measured by the ^{2}D detector and the ^{1}D chromatogram that is reconstructed from a series of ^{2}D chromatograms, as well as the timing information provided by the modulator. There are a few major drawbacks in the conventional GC×GC. First, there is a dilemma in modulation frequency (*i.e.*, ^{1}D sampling rate). On one hand, accurate reconstruction of the ^{1}D chromatogram requires a shorter modulation time (*i.e.*, a higher ^{1}D sampling rate). On the other hand, ^{2}D separation prefers to have a longer modulation time to improve ^{2}D separation and avoid a potential wrap-around issue. A long modulation time (*i.e.*, a low ^{1}D sampling rate) results in distorted peak profiles, additional peak broadening, inaccurate peak retention times, and missing peaks in ^{1}D, which in turn reduces the overall peak capacity for GC×GC and adversely affects peak identification and quantification. In addition, since the relative positions of the ^{1}D peaks and the modulation time cannot be accurately controlled, a phase drift between the ^{1}D peaks and the sampling time point may occur from run to run, which affects the repeatability in ^{1}D chromatogram reconstruction.

Here we propose and develop a new GC×GC configuration and the associated algorithm by inserting an additional non-destructive vapor detector at the end of the ^{1}D column to monitor the ^{1}D eluents (Figure 15(B)). This configuration has several advantages. First, the ^{1}D sampling rate, which now becomes independent of the modulation frequency (usually 0.1-1 Hz), can be as high

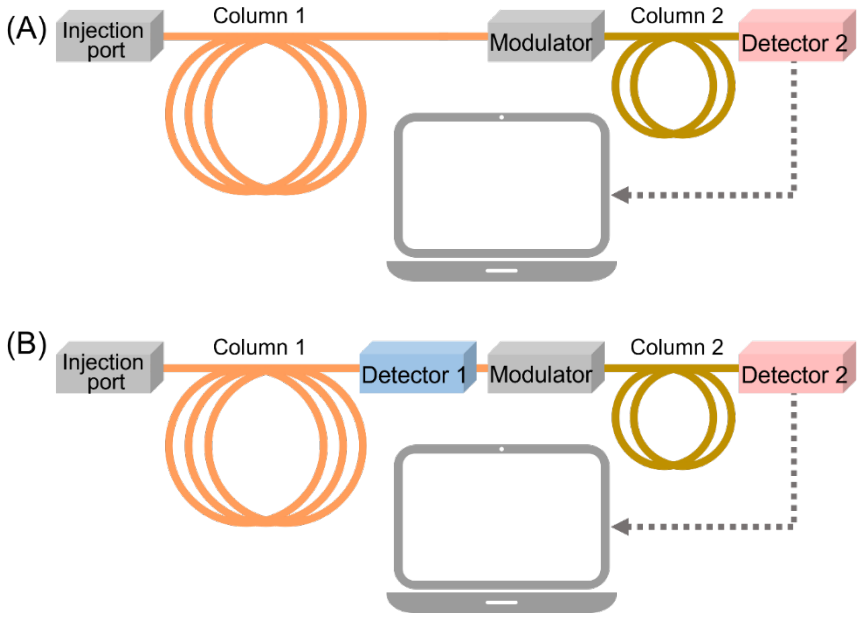

Figure 15. (A) Conventional comprehensive 2-dimensional GC (GC x GC) configuration, where only a ^{2}D detector is used at the end of the ^{2}D column. (B) New GC x GC configuration, where an additional ^{1}D detector is used at the end of the ^{1}D column.

as the detector allows (for example, 100 Hz). Second, instead of reconstructing the ^{1}D chromatogram using the ^{2}D detector signal, the ^{1}D chromatogram can be obtained directly from the ^{1}D detector with a high accuracy. Finally, due to the high ^{1}D sampling rate, the phase drift between the peak position and the modulation time points no longer exists (or significantly reduced). All these result in accurate and repeatable 2D chromatograms, improved peak capacity and peak quantification, and better ability to capture missing peaks. In this paper, we will first introduce the theory and algorithm, followed by systematic investigation of the effects of modulation time, modulation phase, and ^{1}D/^{2}D detector responsivity on GC×GC performance.

As illustrated by Step 1 in the left panel of Figure 16, the output from the ^{2}D detector is sliced according to the modulation time, and each sliced ^{2}D chromatogram is stacked side-by-side along the ^{1}D time axis with the grids defined by the modulation time. In Step 2, the chromatogram is smoothened by interpolation of data points between the ^{2}D chromatogram slices along the ^{1}D axis to obtain a contour plot, as shown in Step 2 in the left panel of Figure 16. Five different interpolation methods were recently compared by Allen and Rutan [6], showing nearly equal performance. In the current work, the modified Akima piecewise cubic Hermite interpolation as implemented in the “interp2” command in MATLAB was used to avoid the overshooting problem found in the spline fitting.

The right panel of Figure 16 describes the procedures of our proposed new differential calibration method for the GC×GC configuration in Figure 15(B). Similar to the conventional procedures, there are two major steps involved. Step 1 is to generate stacked ^{2}D chromatograms along the ^{1}D time axis and Step 2 is to use well-established interpolation algorithms or software built-in functions to create a contour plot. The major difference between our method and the conventional one is that our method can generate stacked ^{2}D chromatograms along the ^{1}D time axis with much finer steps that are determined by the ^{1}D detector sampling rate (rather than the modulation time as in the conventional method). The details of Step 1 in our method are described as follows.

Step 1. Generation of stacked ^{2}D chromatograms along the ^{1}D time axis.

Step 1A. The ^{2}D chromatograms obtained with the ^{2}D detector are sliced according to the modulation time, and each sliced ^{2}D chromatogram is stacked side-by-side along the ^{1}D time axis

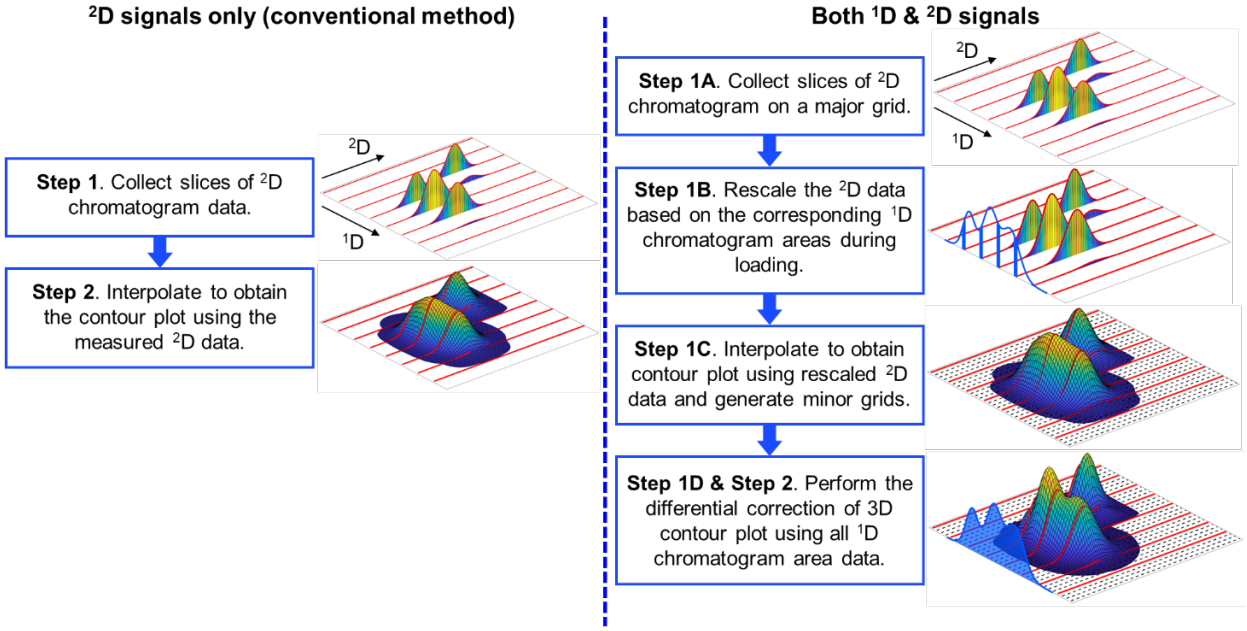

Figure 16. (Left) Conventional method to obtain a 2D chromatogram. (Right) New method to obtain a 2D chromatogram (red lines: major grids; black dashed lines: minor grids).

with the major grids defined by the modulation time. This step is exactly the same as Step 1 in the conventional method.

Step 1B is to rescale the ^{2}D chromatograms based on the ^{1}D chromatogram. Each ^{2}D chromatogram on a major grid is supposed to be produced by a slice of the ^{1}D chromatogram injected into the ^{2}D column due to mass conservation.

Step 1C is to interpolate based on the rescaled ^{2}D chromatograms and generate more ^{2}D chromatograms along the ^{1}D time axis with the minor grids defined by the ^{1}D sampling rate. As illustrated in the right panel of Figure 16, more grids can be added to the original grides that are defined by the modulation time. Assuming that the ^{1}D sampling rate is ^1f Hz, then each fine (or minor) grid has a time interval of $^1t=1/^1f$ seconds. Note that ^1t should be much smaller than the modulation time (for example, ^1t=0.01 s; modulation time=4 s). The corresponding ^{2}D chromatograms on these minor grids can be obtained by interpolation of data points between the ^{2}D chromatograms on the major grids. Any interpolation methods should work. For the sake of convenience, we can use the modified Akima piecewise cubic Hermite interpolation as described previously. Note that this step is very similar to Step 2 in the conventional method. As a result, a series of ^{2}D chromatograms, $^2S_k(t)$, are generated, where m represents the kth grid (including both major and minor grids) that has a ^{1}D time stamp of $k\times{}^1t$.

Step 1D is to rescale all the ^{2}D chromatograms on the major and minor grids based on the ^{1}D chromatogram. Each ^{2}D chromatogram on a major or minor grid is supposed to be produced by a slice of the ^{1}D chromatogram injected into the ^{2}D column. However, except those on the major grids that are obtained directly from the ^{2}D detector, all ^{2}D chromatograms on the minor grids are produced by interpolation in Step 1C. Therefore, we need to rescale all ^{2}D chromatograms using the ^{1}D chromatogram as guidance. For a ^{2}D chromatogram, $^2S_n(t)$, on a major grid at t_n, where t_n is the start time of this modulation, the total quantity of the analytes injected into the ^{2}D column is proportional to the area under the ^{1}D chromatogram measured by the ^{1}D detector, ^{1}S (t), within this modulation period, *i.e.*,

$$^1A_n = \int_{t_n}^{t_n+t_L} {}^1S\ \ (t)dt, \tag{1}$$

where t_L is the ^{1}D-to-^{2}D loading time ($0<t_L<=P_M$ for a pneumatic modulator and $t_L=P_M$ for a thermal modulator, where P_M is the modulation time). On the other hand, assuming that there is no wrap-around issue in ^{2}D separation, the total quantity of analytes detected by the ^{2}D detector should be proportional to the total area under $^2S_n(t)$, *i.e.*,

$$^2A_n = \int_0^{P_M} {}^2S_n(t)dt, \tag{2}$$

where $^2S_n(t)$ is the ^{2}D chromatogram measured by the ^{2}D detector during the nth modulation period. Due to mass conservation, a rescaling factor, R_n, for this modulation period can be obtained as:

$$R_n = \frac{^1A_n}{^2A_n}. \tag{3}$$

Accordingly, $^2S_n(t)$ for this modulation can be rescaled to:

$$^2C_n(t) = R_n \times {}^2S_n(t) \tag{4}$$

We can apply the same technique to the ^{2}D chromatograms on the minor grids.

$$^1A_m = \int_{t_m}^{t_m+t_L} {}^1S\ \ (t)dt, \tag{5}$$

where t_m is the mth grid, $^1S(t)$ is the ^{1}D chromatogram directly measured by the ^{1}D detector.

$$^2A_m = \int_0^{P_M} {}^2S_m(t)dt. \tag{6}$$

Note that Eq. (6) is the same as Eq. (2), except that ^2S_m (t) is not obtained directly from the ^{2}D detector, but by the interpolation described in Step 1B. Accordingly, $^2S_m(t)$ for the mth grid can be

rescaled to:

$$^2C_m(t) = R_m \times {}^2S_m(t), \quad (7)$$

where R_m is

$$R_m = \frac{^1A_m}{^2A_m}. \quad (8)$$

After Step 1D, a series of ^{2}D chromatograms, which are rescaled or calibrated by the ^{1}D chromatogram, are stacked side-by-side along the ^{1}D time axis on the grids much finer than in Figure 16.

Step 2 is the same as Step 2 in the conventional procedures. Interpolation methods (such as "interp2" command in MATLAB used in our current work) are used to generate the contour plot.

In the left panel of Figure 17, different ^{2}D chromatograms (red lines) with varied modulation times (1 s, 2 s, and 3 s) and phase shifts were generated for the same ^{1}D peak (blue lines) using artificial data. The reconstructed contour plots using the conventional and our method are shown on the right panel. The detailed features (symmetry level, ^{1}D retention time $t_{r,\,1D}$, peak volume, and half peak width $W_{1/2}$) of each reconstructed peak in the 2D contour plots are summarized in Table 2.

P_M (sec)	Φ (sec)	Symmetry level		$t_{r,\,1D}$(sec)		Peak volume		$W_{1/2}$(sec)	
		Conv.	New	Conv.	New	Conv.	New	Conv.	New
1	0.6	lightly asymmetrical (L)	highly symmetrical	34.93	35	0.758	0.7	2.63	2.6
	0.4	symmetrical		35.01		0.758		2.62	
	0.2	lightly asymmetrical (R)		35.07		0.758		2.64	
	0.9	symmetrical		34.99		0.758		2.67	
2	0.3	highly asymmetrical (L)		34.35		0.752		3.23	
	1.9	symmetrical		35.07		0.750		3.72	
	1.3	highly asymmetrical (R)		35.40		0.755		2.67	
	0.9	symmetrical		34.97		0.757		2.47	
3	1	highly asymmetrical (L)		34.05		0.715		3.47	
	0.4	symmetrical		35.19		0.649		5.46	
	2.8	highly asymmetrical (R)		35.89		0.726		3.40	
	1.9	symmetrical		34.97		0.856		3.08	

Table 2. Features (symmetry level, ^{1}D retention time, peak volume, and peak width) of reconstructed contour plots corresponding to the artificially generated peaks with different modulation times P_M and phase shifts j.
$t_{r,\,1D}$: ^{1}D retention time at the peak apex.
Peak volume: Volume under a peak in the contour plot.
$W_{1/2}$: Peak width at half maximum of the ^{1}D projection of the peak in the contour plot.

In Figure 17, a symmetric Gaussian peak in ^{1}D is modulated and part of the peak is sent to ^{2}D. For each modulation time, two ^{2}D chromatograms with different phase shifts are presented, one with in-phase modulation (φ = 0.6 s for P_M = 1 s, 0.3 s for P_M = 2 s, and 1 s for P_M = 3 s) the other with out-of-phase modulation (φ = 0.4 s for P_M = 1 s, 1.9 s for P_M = 2 s and 0.4 s for P_M = 3 s). "In-phase" modulation and "out-of-phase" modulation refer to the modulation time are symmetrically and asymmetrically located with respect to the ^{1}D peak apex. As can be seen from the contour plots using the conventional method, the in-phase modulation produces symmetric peaks while the out-of-phase modulation produces asymmetric ones. With the increased modulation time (or the decreased modulation ratio, defined as the ratio between the width of the

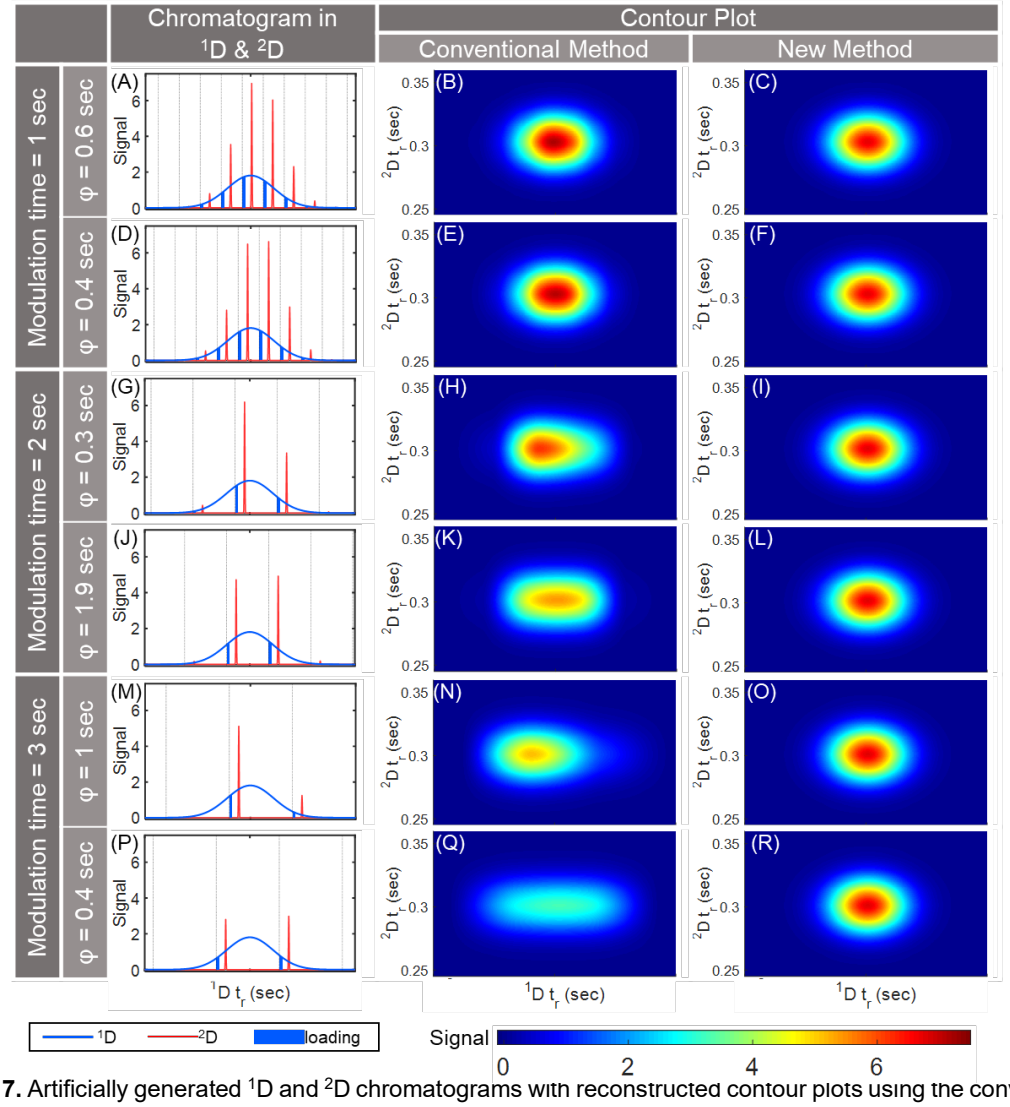

Figure 17. Artificially generated ^{1}D and ^{2}D chromatograms with reconstructed contour plots using the conventional method and the new method, illustrating the influence of modulation time and phase shift. The blue and red curves represent the chromatograms along ^{1}D and ^{2}D, respectively. The blue bars mark the areas under the ^{1}D peaks during ^{1}D-to-^{2}D loading sessions. The ^{1}D peak profiles are the same for all cases. Modulation time and phase shift are varied for ^{2}D and loading times are kept the same for all cases.

^{1}D peak to the modulation time), the reconstructed contour plot becomes less and less accurate with the reconstructed ^{1}D retention time (defined as the peak apex) shifted from its original apex and generally enlarged peak volumes and peak widths, as shown in Figure 17, and Table 2. Therefore, there is a general broadening effect as the modulation time increases by comparing the “Conv.” column to the “New” column in Table 2. Theoretically, the ^{1}D peak broadening can be explained by the sampling theory. Generally, the longer the modulation time is (or the lower the modulation frequency is), the less accurate the reconstructed contour plot is. Using the conventional method with onl y ^{2}D data inevitably introduces peak apex shift, peak broadening, and peak profile distortion, thus reducing the overall GC×GC peak capability and quantification accuracy. In contrast, the new method can obtain consistent contour plots with identical retention time, peak volume, and half peak width, as shown in Figure 17, because they are calibrated using the same ^{1}D chromatogram data. It should be noted that a ^{1}D detector was used previously in 2D assisted liquid chromatography (2DALC), along with a ^{2}D detector. In that arrangement, the

^{2}D data was only used to help better resolve and hence quantify the ^{1}D peaks. In contrast, our method is to use the ^{1}D data to fully calibrate the ^{2}D chromatogram, thus correcting the entire 2D chromatogram (*i.e.*, the contour plot).

Figure 18 presents the artificially generated ^{1}D and ^{2}D chromatograms with coelution, as well as the contour plots from the conventional method and the new method. It is shown that the reconstructed contour plot by the conventional method using the ^{2}D chromatograms alone identified only a single peak, failing to deconvolute the coeluted peaks in the ^{1}D chromatogram. This is because the modulation misses sampling the peak apex or the valley in coeluted peaks, as demonstrated in Figure 18(A). To further separate coeluted peaks in the contour plots, complicated deconvolution methods/algorithms, such as the Parallel factor analysis (PARAFAC) or the Multivariate Curve Resolution-Alternating Least Squares (MCR-ALS) method, are adopted in previous studies. But they may still not able to completely resolve the coelution issue. In contrast, the contour plot in Figure 18(C) using our method clearly shows two separated peaks, demonstrating the superior ability of our new method in handling ^{1}D coelution, which helps recover missed peaks and hence improve the overall GC x GC resolution or peak capacity.

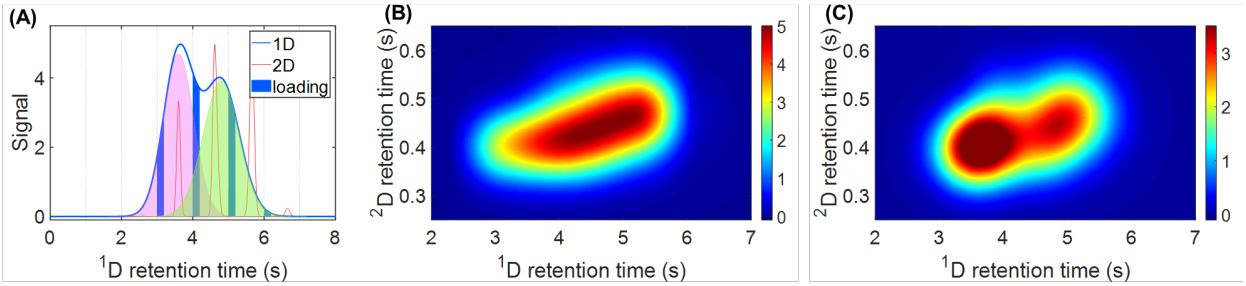

Figure 18. (A) Artificially generated ^{1}D and ^{2}D chromatograms with ^{1}D coelution. (B) Reconstructed contour plot with the conventional method. (C) Reconstructed contour plot with the new method.

Another advantage of using the ^{1}D chromatogram data to calibrate the contour plot is that it makes the reconstructed contour plots immune to detector responsivity changes. Up till now (Figures 17 and 18), we have assumed that ^{1}D and ^{2}D detectors are identical. In real-world scenarios, the ^{1}D and ^{2}D detectors may have different responsivities even to the same analyte (such as photoionization detector – PID, and flame ionization detector - FID). To demonstrate the robustness of the new method with varying responsivity ratios between the ^{1}D and ^{2}D detectors, three scenarios with different ^{1}D and ^{2}D detector responsivity ratios were generated as shown in Figure 19 and Table 3. Other than the responsivity ratios, all the other peak features were kept the same for the three scenarios.

	Control		Same type of detector in ^{1}D and ^{2}D		Different types of detectors in ^{1}D and ^{2}D	
	Species A	Species B	Species A	Species B	Species A	Species B
^{1}D t_r (sec)	35	45	35	45	35	45
^{2}D t_r (sec)	0.3	0.5	0.3	0.5	0.3	0.5
^{1}D $W_{1/2}$ (sec)	2.6	3	2.6	3	2.6	3
^{2}D $W_{1/2}$ (sec)	0.035	0.03	0.035	0.03	0.035	0.03
^{1}D area (unitless)	5	3	5	3	5	3
Responsivity ratio	1:1	1:1	1:0.7	1:0.6	1:0.5	1:1.2

Table 3. Peak features for reconstructed contour plots with different detector responsivity ratios.

In our modeling, the ^{1}D detector has a responsivity 5 and 3 to Species A and B, respectively. In the first row of Figure 19, we assume that the ^{2}D detector is of the same type as the ^{1}D detector and therefore has the responsivity of 5 and 3 to Species A and B, too. Note the absolute responsivity of the ^{2}D detector changes proportionately (for example, responsivity to Species A and B increases to 10 and 6), it does not change the 2D contour plot and the results due to the ratio metric nature between the ^{1}D and ^{2}D detection of our method (see Eqs. (3) and (8)). This row is used as a control, where both the conventional and our method are able to see two peaks in the 2D contour plot with accurate quantification (or peak volume).

The second row simulates the scenario where the ^{1}D and ^{2}D detectors have different responsivities to Species A and B, but both ^{1}D and ^{2}D have a higher responsivity to Species A than to Species B (*i.e.*, ^{1}D detector has responsivity of 5 and 3 to Species A and B, respectively, whereas ^{2}D detector has a responsivity of 3 and 2 to Species A and B, respectively). The third row simulates the scenario where the ^{2}D detector has a responsivity of 2 to Species A, lower than its responsivity (=3) to Species B. In both scenarios, the conventional method yields peaks with different peak volumes and width, whereas our method yields consistent peak features. This is because all the changes in the contour plots due to the ^{2}D detector ratio change are rescaled according to the original ^{1}D detector responsivity ratio. Our method enables high versatility in detector selection. For example, we can choose PID/PID as the ^{1}D and ^{2}D detectors, or PID/FID as the ^{1}D and ^{2}D detectors.

Furthermore, the above discussion also suggests that we can afford some mass loss in the ^{1}D detector. In our previous discussion, we have assumed that the ^{1}D detector is non-destructive. But now, based on our results in Figure 19, we can use a ^{1}D detector that may have some mass loss (*i.e.*, minimally destructive detector rather than non-destructive detector) The mass loss scenario can be understood as ^{1}D and ^{2}D showing different responsivities. For example, with a 10% mass loss, the absolute responsivity of ^{1}D and ^{2}D detector becomes 5:3 vs. 4.5:2.7 (for the first row in Figure 19) and 5:3 vs. 2.7:1.8 (for the second row in Figure 19). The scaling factor introduced by the mass loss can be easily corrected after rescaling with the ^{1}D data, as long as the mass loss is not too high to hide all ^{2}D signals below the baseline noise level.

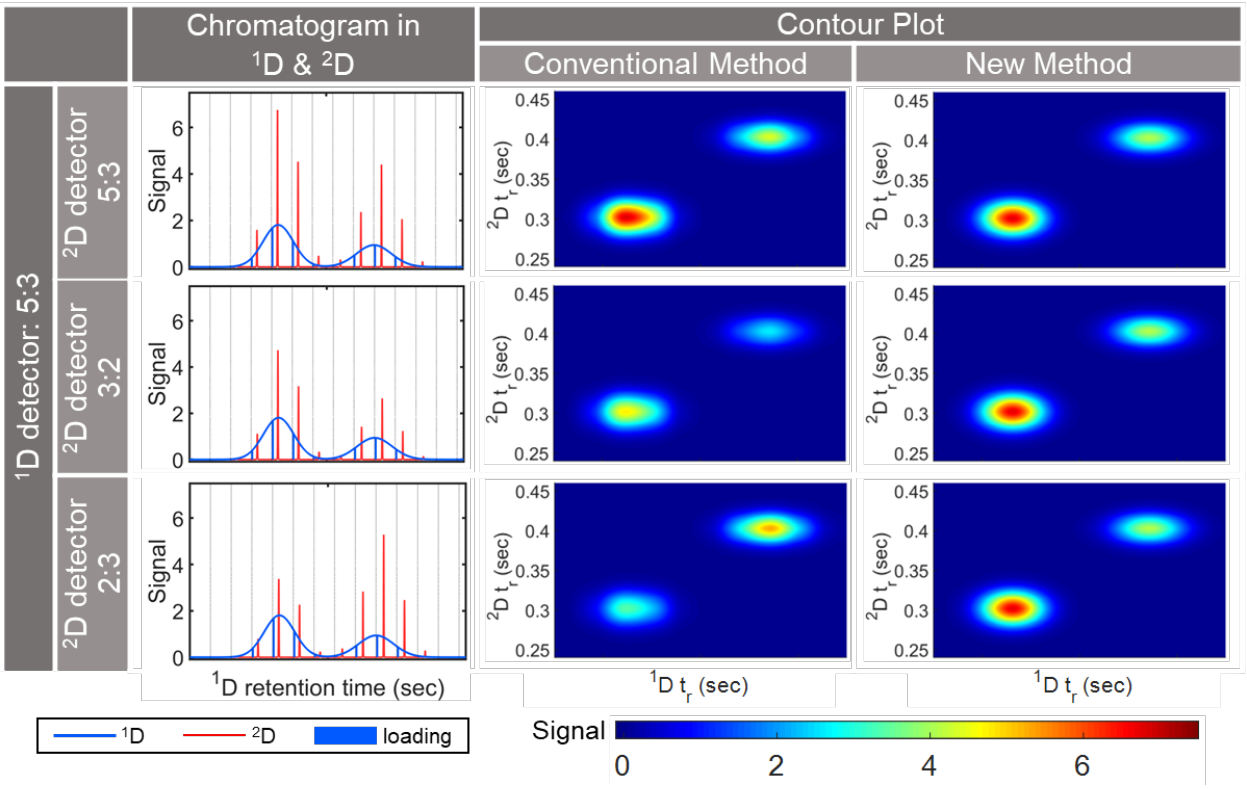

Figure 19. Generated ^{1}D and ^{2}D chromatograms with different ^{1}D and ^{2}D detector responsivity ratios and their corresponding reconstructed contour plots using the conventional method and the new method.

B.2 (Accomplishments.pdf)

4. Technology transfer

We have been working with the University of Michigan Innovation Partnerships (also known as the Office of Tech Transfer) to find the best strategies to commercialize the technologies developed through the proposed project. To date, we have filed/obtained 6 disclosures/patents (see Invention Statement). Some of them have been licensed to third-party companies.

C. PRODUCTS

C.1 PUBLICATIONS

Are there publications or manuscripts accepted for publication in a journal or other publication (e.g., book, one-time publication, monograph) during the reporting period resulting directly from this award?

No

C.2 WEBSITE(S) OR OTHER INTERNET SITE(S)

NOTHING TO REPORT

C.3 TECHNOLOGIES OR TECHNIQUES

NOTHING TO REPORT

C.4 INVENTIONS, PATENT APPLICATIONS, AND/OR LICENSES

Have inventions, patent applications and/or licenses resulted from the award during the reporting period? Yes

If yes, has this information been previously provided to the PHS or to the official responsible for patent matters at the grantee organization? Yes

C.5 OTHER PRODUCTS AND RESOURCE SHARING

Category	Explanation
Other	The team has the following publications. They could not be found in C1. Maxwell Wei-Hao Li, Abhishek Ghosh, Anandram Venkatasubramanian, Ruchi Sharma, Xiaolu Huang, and Xudong Fan, "High-Sensitivity Micro-Gas Chromatograph–Photoionization Detector for Trace Vapor Detection," ACS Sensors 6, 2348-2355 (2021). Xiaheng Huang, Maxwell Wei-hao Li, Wenzhe Zang, Xiaolu Huang, Anjali Devi Sivakumar, Ruchi Sharma, and Xudong Fan, "Portable Comprehensive Two Dimensional Micro-Gas Chromatography Using Integrated Flow-Restricted Pneumatic Modulator," Nature Microsystems & Nanoengineering 8, 115 (2022). Xiaheng Huang, Ruchi Sharma, Anjali Devi Sivakumar, Shuo Yang, and Xudong Fan, "Ultrathin silica integration for enhancing reliability of microfluidic photoionization detectors," Analytical Chemistry 95, 8496–8504 (2023). Wenzhe Zang, Ruchi Sharma, Maxwell Wei-Hao Li, and Xudong Fan, "Retention time trajectory matching for target compound peak identification in chromatographic analysis,"

	Sensors 23, 6029 (2023). Wenzhe Zang, Xiaheng Huang, Ruchi Sharma, and Xudong Fan, "Differential Calibration of Contour Plot Using 1D Data in Comprehensive Two-Dimensional Gas Chromatography," to be submitted. Xiaheng Huang and Xudong Fan, "Avalanche photoionization detector," to be submitted. Xiaheng Huang, Wencheng Li, Shuo Yang, Ruchi Sharma, Anjali Devi Sivakumar, Robert Nidetz, Hongbo Zhu, Weishu Wu, Seong-Yong Jeong, and Xudong Fan, "Monolithically integrated micro-PID on µcolumns for ultracompact micro-gas chromatography," to be submitted.

D. PARTICIPANTS

D.1 WHAT INDIVIDUALS HAVE WORKED ON THE PROJECT?

Commons ID	S/K	Name	Degree(s)	Role	Cal	Aca	Sum	Foreign Org	Country	SS
FANXUD	Y	Fan, Xudong	BS,MS,PHD	PD/PI	0.0	0.5	0.5			NA
RJRICH	N	RICHARDSON, RUDY J	MOTH,SCD	Co-Investigator	0.4	0.0	0.0			NA
RNEITZEL	N	Neitzel, Richard L	BS,MS,PHD	Co-Investigator	0.0	0.6	0.2			NA
KATSUO	N	Kurabayashi, Katsuo	PHD	Co-Investigator	1.4	0.0	0.0			NA
LAUMARIE	N	Smith, Lauren Marie	BS,MPH,MS	Research Area Specialist Sr	0.9	0.0	0.0			NA
YGPARK	N	Park, Young Geun		ASST RES SCIENTIST	2.4	0.0	0.0			NA
MAXLI1	N	Li, Maxwell		Postdoctoral Scholar, Fellow, or Other Postdoctoral Position	2.9	0.0	0.0			NA
XIAHENG1	N	Huang, Xiaheng	PHD,MS,BS	Graduate Student (research assistant)	2.0	0.0	0.0			NA
AFARAHAN	N	Tabartehfarahani, Ali	PHD	Postdoctoral Scholar, Fellow, or Other Postdoctoral Position	2.0	0.0	0.0			NA
	N	Zhang, Xin		Research Area Specialist Assoc	10.7	0.0	0.0			NA

Glossary of acronyms:
S/K - Senior/Key
Cal - Person Months (Calendar)
Aca - Person Months (Academic)
Sum - Person Months (Summer)
Foreign Org - Foreign Organization Affiliation
SS - Supplement Support
RS - Reentry Supplement
DS - Diversity Supplement
OT - Other
NA - Not Applicable

D.2 PERSONNEL UPDATES

D.2.a Level of Effort

Not Applicable

D.2.b New Senior/Key Personnel

Not Applicable
D.2.c Changes in Other Support Not Applicable
D.2.d New Other Significant Contributors Not Applicable
D.2.e Multi-PI (MPI) Leadership Plan Not Applicable

E. IMPACT

E.1 WHAT IS THE IMPACT ON THE DEVELOPMENT OF HUMAN RESOURCES?
Not Applicable
E.2 WHAT IS THE IMPACT ON PHYSICAL, INSTITUTIONAL, OR INFORMATION RESOURCES THAT FORM INFRASTRUCTURE?
NOTHING TO REPORT
E.3 WHAT IS THE IMPACT ON TECHNOLOGY TRANSFER?
Not Applicable
E.4 WHAT DOLLAR AMOUNT OF THE AWARD'S BUDGET IS BEING SPENT IN FOREIGN COUNTRY(IES)?
NOTHING TO REPORT

G. SPECIAL REPORTING REQUIREMENTS SPECIAL REPORTING REQUIREMENTS

G.1 SPECIAL NOTICE OF AWARD TERMS AND FUNDING OPPORTUNITIES ANNOUNCEMENT REPORTING REQUIREMENTS

NOTHING TO REPORT

G.2 RESPONSIBLE CONDUCT OF RESEARCH

Not Applicable

G.3 MENTOR'S REPORT OR SPONSOR COMMENTS

Not Applicable

G.4 HUMAN SUBJECTS

G.4.a Does the project involve human subjects?

Not Applicable

G.4.b Inclusion Enrollment Data

NOTHING TO REPORT

G.4.c ClinicalTrials.gov

Does this project include one or more applicable clinical trials that must be registered in ClinicalTrials.gov under FDAAA?

G.5 HUMAN SUBJECTS EDUCATION REQUIREMENT

NOT APPLICABLE

G.6 HUMAN EMBRYONIC STEM CELLS (HESCS)

Does this project involve human embryonic stem cells (only hESC lines listed as approved in the NIH Registry may be used in NIH funded research)?

No

G.7 VERTEBRATE ANIMALS

Not Applicable

G.8 PROJECT/PERFORMANCE SITES

Not Applicable

G.9 FOREIGN COMPONENT
No foreign component
G.10 ESTIMATED UNOBLIGATED BALANCE
Not Applicable
G.11 PROGRAM INCOME
Not Applicable
G.12 F&A COSTS
Not Applicable

I. OUTCOMES

I.1 What were the outcomes of the award?

Project: "Novel gas chromatography for rapid, in situ workplace hazardous VOC/VIC analysis"
Contact PI: Xudong Fan
Organization: University of Michigan

Rapid and sensitive detection and analysis of toxic gases is of paramount importance to human health. A field-deployable gas analyzer is highly desirable to help analyze low concentrations of those chemicals in real-time.

Through the project, a miniature device called micro-gas chromatography (micro-GC) is developed and constructed. First, all the related components are microfabricated and tested. Second, a highly sensitive detector is developed to detect gas concentrations in the range of parts-per-trillion. Furthermore, the detector's lifetime is significantly extended to make the detector more practical. Finally, a few automated battery-powered micro-GC devices are constructed with an unprecedented size and weight, which can be as low as 0.88 L and 900 g (including the battery box). Gas analysis can be completed in 10 minutes. To further help analyze gas molecules, two algorithms are developed to provide better gas separation ability and gas identification ability. The hardware and algorithms are ready to be translated to industrial companies for further commercialization development.